CALIBRATION AND CHARACTERIZATION OF A VNIR HYPERSPECTRAL IMAGER FOR PRODUCE MONITORING

by

Riley Donovan Logan

A professional paper submitted in partial fulfillment
of the requirements for the degree

of

Master of Science

in

Optics and Photonics

MONTANA STATE UNIVERSITY
Bozeman, Montana

May 2020

ACKNOWLEDGEMENTS

The work presented here was funded by the Intel Corp. under Agreement Montana-Intel SRA 10-18-17 with additional funding provided in part by the National Science Foundation EPSCoR Cooperative Agreement OIA-1757351 and completed on the Montana State University – Bozeman campus. I would like to extend my thanks to everyone who contributed to this work and provided much needed help, explanations, and encouragement. Namely, I would like to thank the members of the Numerical Intelligent Systems Laboratory at Montana State University – Bozeman, including Jacob Senecal, Neil Walton, Amy Peerlinck, and Dr. John Sheppard for all their excellent contributions. Additionally, I would like to thank the members of the Optical Remote Sensor Laboratory for their support, laughter, and advice. I consider myself very lucky to have the opportunity to work with such talented and kind people every day. I was fortunate to have an incredible set of mentors on my committee for this work – thank you to Dr. Wataru Nakagawa, Dr. Charles Kankelborg, and my advisor, Dr. Joseph Shaw, for the many hours of advice, teaching, and patience in dealing with my questions. Finally, I would like to extend a thank you to my parents, Jill and Jeff Logan, who have always given me unquestionable support.

TABLE OF CONTENTS

TABLE OF CONTENTS – CONTINUED

LIST OF TABLES

LIST OF FIGURES

LIST OF FIGURES – CONTINUED

Figure Page

LIST OF FIGURES – CONTINUED

ABSTRACT

Hyperspectral imaging is a powerful remote sensing tool capable of capturing rich spectral and spatial information. Although the origins of hyperspectral imaging are in terrestrial remote sensing, new applications are emerging rapidly. Owing to its non-destructive nature, hyperspectral imaging has become a useful tool for monitoring produce ripeness. This paper describes the process of characterizing and calibrating a visible near-infrared (VNIR) hyperspectral imager for obtaining accurate images of produce to be used in machine learning algorithms for analysis. In this work, many calibrations and characterization are outlined, including: a radiance calibration, the process of calculating reflectance, pixel uniformity and image stability testing, spectral characterization, illumination source analysis, and measurement of the polarization response. The images obtained by the calibrated hyperspectral imager were converted to reflectance across a spectral range of 387.12 nm to 1023.5 nm, with a spectral resolution of 2.12 nm. A convolutional neural network was used to perform age classification for Yukon Gold potatoes, bananas, and green peppers. Additionally, a genetic algorithm was used to determine the wavelengths carrying the most useful information for age classification. Experiments were run using red green blue (RGB) images, full-spectrum hyperspectral images, and the wavelengths selected by the genetic algorithm feature selection method. Preliminary data from these analyses show promising results at accurately classifying produce age. The genetic algorithm feature selection method is being used to develop a low-cost multispectral imager for use in monitoring produce in grocery stores.

INTRODUCTION

The Food Waste Problem

In 2011, global food waste was estimated at 1.2 billion metric tons annually, meaning that approximately one-third of all food produced for human consumption was wasted [15, 43]. The United States doesn't fall far from the global average when it comes to food waste, with nearly 113 million metric tons, or roughly 29% of all food produced going to waste [43], with some estimates placing the number as high as 40% [13]. This not only costs businesses and consumers across the United States between $165 and $198 billion annually, [13, 43] but decomposition of wasted food releases greenhouse gasses that contribute to global climate change [16, 26]. Additionally, food waste can be tied to an increased consumption of over one-quarter of freshwater and nearly 300 million barrels of oil [16].

According to the United States Department of Agriculture (USDA), 133 billion pounds of food was wasted at the retail and consumer level in 2010 [3]. The loss of fruits and vegetables in retail grocery stores, from either unsold or discarded produce, amounts to approximately $15 billion annually. This loss is driven by many factors, such as overstocked product displays and damaged goods [13], but can also be attributed to produce becoming overripe on store shelves. Employees at our local grocery stores tell us that damaged or overripe produce is currently identified by employees who survey the display shelves throughout the day, removing produce that appears damaged or overripe. However, human observers are unable to predict when produce may be going bad, meaning produce is discarded once it has already passed the point of prime retail value. The ability to forecast the life cycle of produce would allow retail stores to implement strategies for rapidly selling produce that is about to expire. An emerging technology for detection and monitoring of the produce life cycle is found in hyperspectral imaging.

Optical remote sensing has long been used for non-destructively analyzing food safety and quality, [1, 17, 21, 30, 31] especially hyperspectral imaging, owing to its rich spatial and spectral information. The spectral information available at each pixel is useful for monitoring the ripening of fruits and vegetables, which usually involves chemical processes such as chlorophyll degradation, changes in respiration, biosynthesis of carotenoids, and changes in ethylene production [33]. Many of the visible changes throughout the ripening process are attributed to changes in pigmentation induced by varying chlorophyll content and accumulation of carotenoids. Changes in pigmentation present in produce can be observed with the high spectral resolution of a hyperspectral imaging system, allowing for detection of the ripening cycle. In one such case, hyperspectral imaging was used to observe banana fruit quality and maturity stages at three different temperatures [34]. Using quality parameters such as firmness, moisture content, and total soluble solids, they developed a relationship between quality and spectral data using partial least square analysis. Additionally, important wavelengths were determined using predicted residual error sum of squares, revealing eight visible and near-infrared wavelengths that carried the most information for determining quality.

Machine learning algorithms are commonly used in these applications to process large quantities of data. For example, machine learning methods have been used with machine vision or RGB cameras for classifying and grading the quality of fruits and vegetables [5, 27, 29] and determining the ripeness of bell peppers [8] and gooseberries [4]. Convolutional neural networks have been employed to process images from low-cost RGB cameras coupled to a Raspberry PI computer to identify fruit and vegetable types [9] and to process smartphone images to detect artificially ripened fruit [42].

Machine learning is particularly useful for analyzing the large quantities of spectral data generated by hyperspectral imagers or spectrometers. Some relevant applications include detecting fungi that cause citrus fruit to rot [11], identifying mechanical damage to mangoes [36], classifying produce type [14], and evaluating tomato ripeness [7, 31].

In this paper, I first present calibration and characterization procedures and results for a visible and near-infrared (VNIR) hyperspectral imager. I then present a promising method for detecting and predicting the ripening process of fruits and vegetables using the calibrated hyperspectral imager coupled with machine learning algorithms. My primary contribution to this work was performing the calibration of the hyperspectral imaging system to provide meaningful and reliable data to the team of computer scientists, who performed the machine learning analysis. However, the calibration and characterization procedures presented in this paper go well beyond what was required for the produce ripening study, as explained below.

When capturing an image of a scene, an uncalibrated imaging system will record the detected signal according to its unique optical and electronic response, producing a digital number at each pixel. The digital number recorded by an imaging system is a function of several factors, including sensor responsivity, optical components in the system, and bit depth of the sensor readout. Though measurements recorded in digital numbers can be suitable for standard photography, they cannot be used for scientific measurement or for comparison with other imaging systems due to each imager's unique response. Therefore, imaging systems must be calibrated to express their measurements in terms of a physical quantity that is meaningful for a given sensor and application (e.g., reflectance, radiance, or temperature). There are many ways to calibrate an imaging system, but the calibrations and analyses presented in this paper will focus on a radiance calibration, conversion to reflectance, pixel uniformity testing, image stability analysis, spectral performance testing, and polarization response testing, all for a Resonon Pika L hyperspectral imager [35].

The work presented here focuses on the use of hyperspectral imaging for food safety and food quality analysis; however, the calibrations presented will be helpful in many other areas of research. For example, the Optical Remote Sensor Laboratory at Montana State University utilizes the Pika L hyperspectral imager for applications ranging from precision agriculture [28, 37] to river ecology. In all these applications, calibrations are required to obtain meaningful data. However, to lay the groundwork for the presentation of calibration methods, we must begin with the basics of hyperspectral imaging.

Hyperspectral Imaging

To aid in the understanding of hyperspectral imaging, we will begin with a discussion of the simpler case, multispectral imaging. A multispectral imager is just that - an imaging system capable of capturing multiple spectral bands. The detected bands do not need to be contiguous or within the range of visible wavelengths; however, a common example of a visible-wavelength multispectral imager is the camera contained within the cell phone resting in most of our pockets. These relatively simple systems quantify the amount of radiation incident on a filtered sensor array in each of the RGB spectral bands to recreate the color images we are accustomed to seeing. Hyperspectral imaging, on the other hand, has additional complexities and capabilities.

The line separating multispectral imaging from hyperspectral imaging is not well-defined [22], although hyperspectral imaging is best characterized by recording a contiguous sequence of narrow spectral bands, resulting in a continuous spectrum at each pixel of an image. This typically involves recording hundreds of spectral bands, whereas multispectral imaging typically involves a dozen or fewer spectral bands. The high-resolution spectral information captured by a hyperspectral imager is achieved through the use of some mechanism of optically dispersing the incident light into a complete spectrum. This can be done with a dispersive element like a prism or grating, or with an interferometric approach such as Fourier transform spectroscopy. The Resonon Pika-L imager used in this study relies on a diffraction grating.

Hyperspectral imagers come in many different forms, but for the scope of this paper, only push-broom hyperspectral imagers, such as the Pika L, will be discussed. Push-broom imagers, also known as line-scan imagers, obtain spectral information from a scene one spatial line at a time. The second spatial dimension is obtained by translating the imaging system across the scene, capturing images at a specified frame rate, then stacking each of the imaged frames together. This process is visualized through the example of capturing an image of a hand of bananas (Figure 4.5). Here, the imager is scanned across the bananas, as shown, capturing frames as it is translated. The complete image cube of the hand of bananas is obtained by assembling the individually captured frames. This process results in a two-dimensional image that is typical of an imaging system, with each pixel's value and spatial location given by its x and y coordinates within the image. However, the power of hyperspectral imaging becomes evident upon closer inspection of a single frame.

In Figure 4.5, we see that assembling all frames captured while translating a hyperspectral imager across a scene results in a two-dimensional spatial image. However, each frame captured during this process is itself a two-dimensional image, except instead of consisting of two spatial dimensions (i.e. pixel location in Cartesian coordinates), the frame is comprised of a spatial and a spectral dimension. This principle is illustrated in Figure 1.2, where a single frame captured during the

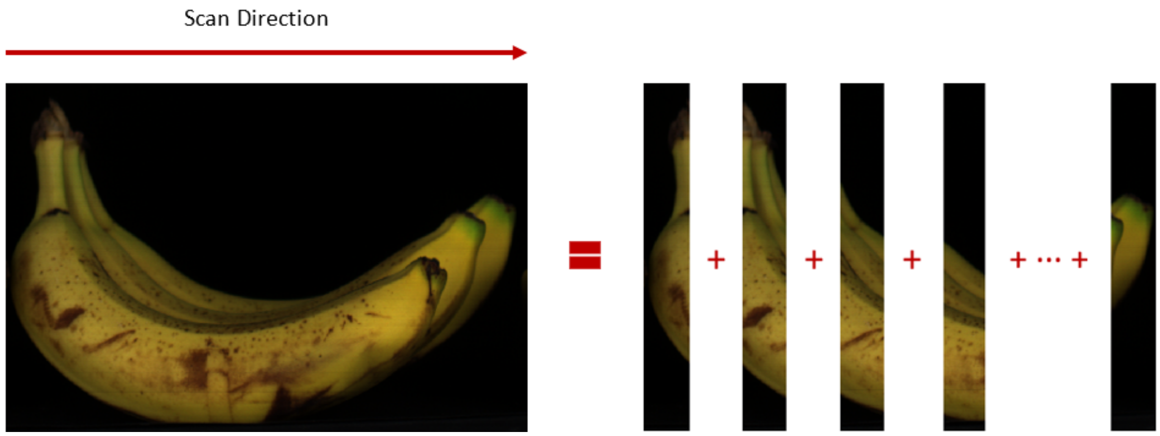

Figure 1.1: Example of image capture for a push broom style imager. A complete image is obtained by combining individually scanned lines, shown at exaggerated sizes.

translation process is shown with exaggerated individual pixels labeled. At each pixel, the full spectrum captured by the imaging system is available.

Combining the two principles outlined above, a two dimensional image is formed with many spectral layers. At each of these spectral layers, the same spatial image is formed (i.e. Figure 4.5) where the full spectrum detected by the imager is available at each pixel (i.e. Figure 1.2). This results in a three-dimensional image, where two axes represent spatial locations of pixels and the third axis represents the spectral layers contained in the image (Figure 1.3). The spectral dimension represents the number of spectral channels captured by the imaging system. For example, if an imaging system captures 300 spectral channels across the spectral range of 400 nm to 1000 nm, the spectral axis will take on the same range and consist of 300 layers, each separated by 2 nm. The final step in hyperspectral imaging is to combine all of the spectral layers such that they are contiguous. Once this process is complete, a hyperspectral data cube is formed (Figure 1.4).

Hyperspectral data cubes contain rich spectral information, but this wealth of

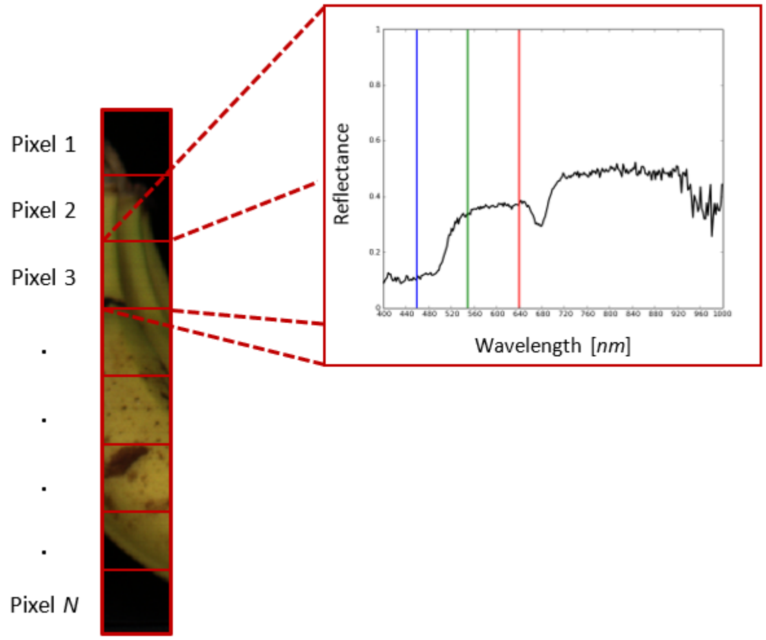

Figure 1.2: Single frame in hyperspectral data cube with exaggerated pixels shown. At each pixel, the full spectrum captured by the imager is available.

information comes at the cost of complex and dense data products. The ability for each pixel to contain a full spectrum means that each pixel is stored as a vector comprised of the measured signal as a function of wavelength. Returning to our previous example, in which we have 300 spectral channels, this means each pixel is represented by a vector containing 300 values. As imaging systems often contain thousands of pixels, analysis and processing of hyperspectral data cubes can quickly become computationally expensive.

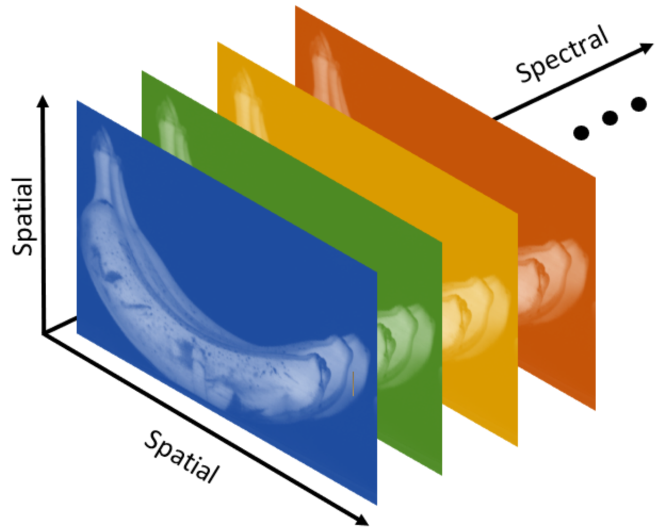

Figure 1.3: Example three-dimensional hyperspectral data cube consisting of two spatial dimensions and one spectral dimension. The spectral dimension extends for the full spectral range of the hyperspectral imager.

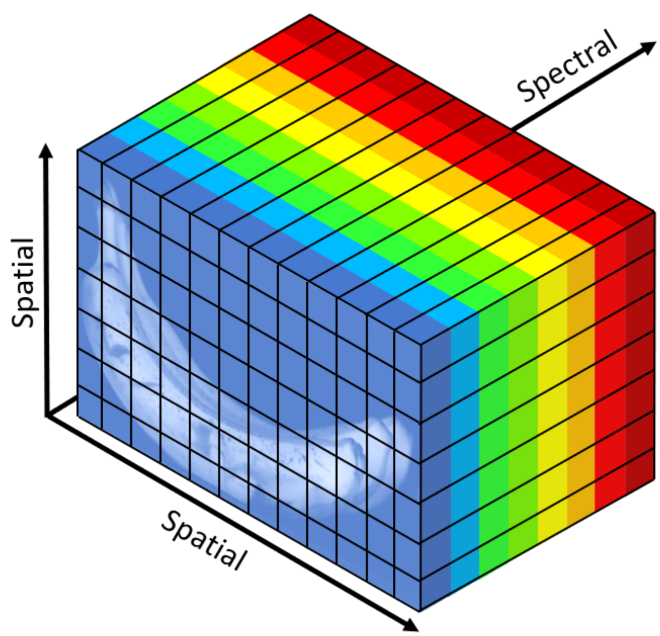

Figure 1.4: Example of a full hyperspectral data cube. The full spectrum captured by the imager is available at each pixel.

CALIBRATION AND CHARACTERIZATION

Background

For an imaging system to collect quantitatively meaningful data, it must first be calibrated and characterized. As presented in Chapter 1, each imaging system records a unique electronic response that is a function of sensor responsivity, optical components in the system, and bit depth of the sensor readout. Sensor responsivity is typically defined as the sensor's ability to convert incident light (measured in watts) to electric signal (i.e. current or voltage). For example, current responsivity, measured in amperes per Watt, can be expressed as

$$R = \frac{\eta q}{h\nu}, \tag{2.1}$$

where η is the quantum efficiency of the detector, or the probability that an incident photon will be converted to an electron; q is the charge of an electron; h is Planck's constant; and ν is the frequency of incident light. Notice that the responsivity varies with frequency (and wavelength) and quantum efficiency. As no two sensors have the exact same quantum efficiency across a given spectral range, and sensors fabricated from different materials can have large differences in their quantum efficiencies, it becomes difficult to make meaningful comparisons between sensors without measuring the spectral response function (Figure 2.1).

Optical components present in the imaging system also play a role in the signal detected by the imager. In addition to the deviations from the perfect focusing performance of an ideal lens, known as aberrations, materials and coatings used to construct the lens also affect the detected signal. This property, known as transmittance, dictates how well certain wavelengths pass through a focusing lens.

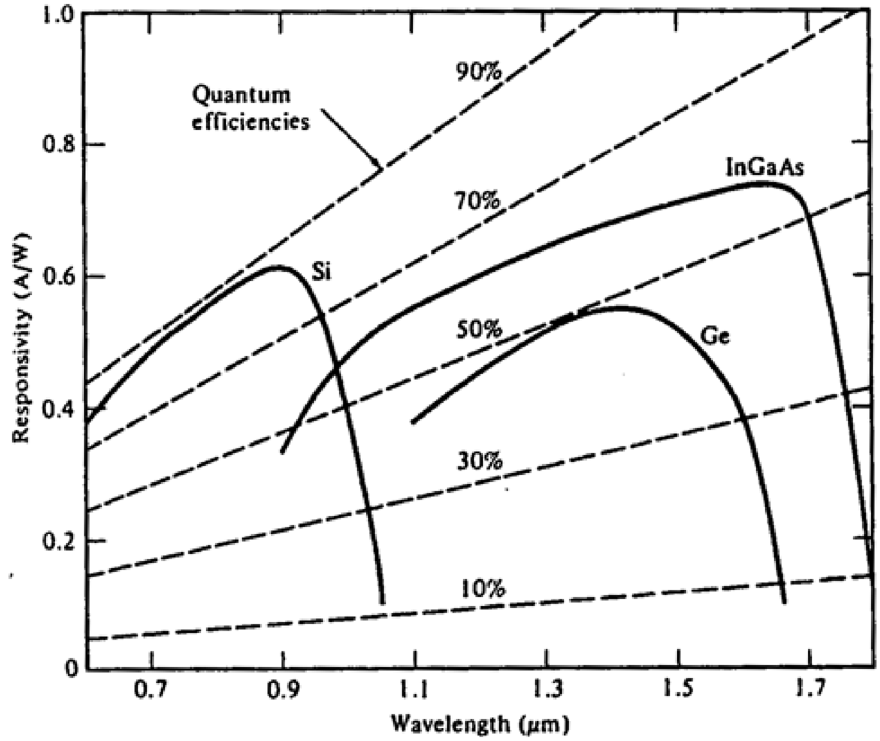

Figure 2.1: Current responsivity curves for several sensor types [10].

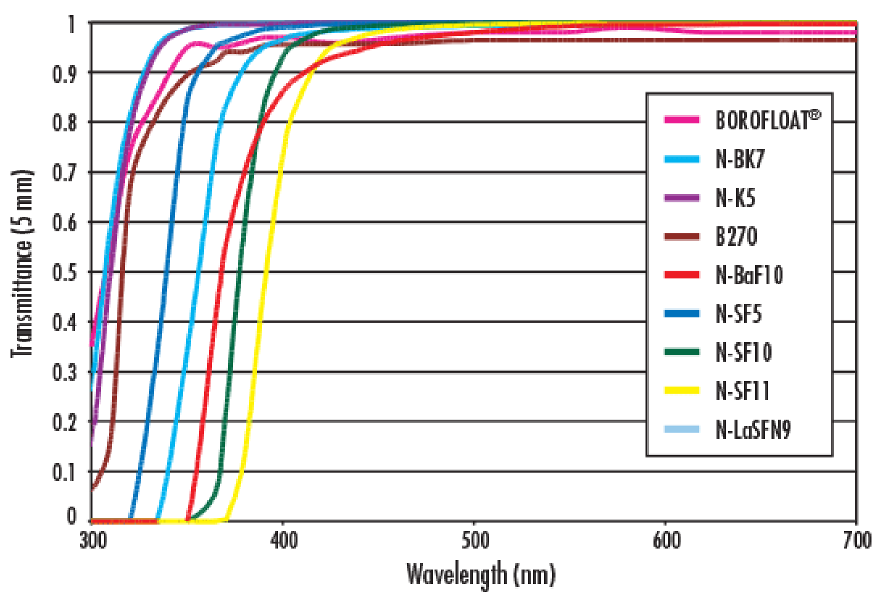

Figure 2.2: Spectral transmittance of several common glass types [6].

Figure 2.2 shows the spectral transmittance of several glass types all with a thickness of 5 mm.

The light that is transmitted through the optical system and detected on a sensor produces an electrical signal, which is often digitized with an analog-to-digital converter (ADC). The bit depth of the ADC determines the range of values its readout can take on. Each bit is stored in a binary fashion (i.e. 0 or 1). The bit depth refers to how many bits are concatenated to store information. For example, a sensor with a bit depth of 2 could output four values (00, 01, 10, 11). This system would have very poor resolution, so imagers generally have much higher bit depths, often above 8. The range of values allowed by an sensor's readout is dictated by 2^n where n is the number of bits available in the sensor. A higher bit depth means an imaging system will record information with higher resolution; however, the range of bit depths offered in imaging systems provides an additional challenge when attempting to compare signals detected between imaging systems. For example, if two imagers simultaneously capture photographs of the same scene, one with a bit depth of 8 and the other with a bit depth of 12, the first imager will report a value between 0-255 while the second will report a value between 0-4095. Comparison between these two hypothetical imagers would be very difficult unless the unique response of each imager had been characterized. The goal of calibration and characterization is therefore to account for not only differences in bit depth, but also all the effects outlined above, so that a measurement is made independent of the sensing instrument insofar as possible.

This chapter presents the methodology and results of a wide array of calibration and characterization measurements performed on a Resonon Pika L hyperspectral imaging system. Before introducing the calibration and characterization procedures, I present the specifications of the imaging system.

Pika L Hyperspectral Imager

The Pika L hyperspectral imager operates across a spectral range of 387.12 nm to 1023.50 nm with a spectral resolution of 2.12 nm, resulting in 300 spectral channels. Image data cubes are captured with a bit depth of 12 across 900 fixed spatial pixels (i.e., the spatial dimension acquired without scanning). Values obtained at each pixel are averaged with neighboring pixels, in a process called binning. By default, the Pika L is set with 2× binning, meaning values are averaged across two pixels, resulting in a 2.12 nm spectral resolution. Full specifications are presented in Table 2.1.

The data products created by the Pika L are three-dimensional data cubes, with dimensions of $900 \times N \times 300$, where 900 is the number of pixels in the first (nonscanning) spatial dimension, N is the second spatial dimension obtained by scanning the imager across a scene, and 300 is the number of pixels in the spectral dimension. Therefore, each pixel in the resulting 900 x N spatial image is comprised of a vector with 300 values, each representing the signal strength of a different spectral layer. This data-oriented view of a hyperspectral image cube will be useful when presenting calibration techniques, as many calibration and characterization procedures presented rely on pixel-by-pixel analysis across all spectral channels.

Radiance Calibration

A radiance calibration refers to the conversion from digital number to the physical units of radiance, measured in watts per square meter per steradian ($Wm^{-2}sr^{-1}$). The need for a radiance calibration arose during the early stages of analyzing the life cycle of produce. As we were searching for a change in spectral features with possibly different lighting conditions, performing a radiance calibration was a natural place to begin.

Table 2.1: Specifications for the Resonon Pika L hyperspectral imager [35]

Pika L Hyperspectral Imager	
Spectral Range	387.12 nm to 1023.50 nm
Spectral Resolution	2.12 nm
Spatial Channels	900
Max Frame Rate	249 fps
Bit Depth	12
Spectral Pixels	600 (2× binning gives 300 spectral channels)
Pixel Size	5.86 µm

The process of completing a radiance calibration is relatively straightforward, but instrumentation with sufficient accuracy and precision must be used. To begin, a steady state, variable light source of known radiance is used for illumination. The illumination must act as an extended source whose aperture fills the field of view of the imaging system being calibrated. A common light source used for calibration in the VIS-NIR-SWIR spectral range is an integrating sphere. These spherical instruments have a high-reflectivity Lambertian internal coating and internal tungsten halogen light source [18]. When the internal light source is turned on, the high-reflectivity coating creates diffuse reflections, which scatter and depolarize the light from the source. After many reflections, the ideal output is randomly polarized, spatially uniform light emitted from an exit aperture. The internal halogen light source is shuttered, allowing for control of emitted radiance. Using an internal photodetector, current is measured and calibrated to radiance according to NIST standards. Our integrating sphere (Labsphere USLR-V12F-NDNN) shows high-spatial uniformity across its exit aperture, with a uniformity of 98.97% (Figure 2.3). Here, uniformity is defined as

$$Uniformity = (1 - (Max - Min)) * 100. \tag{2.2}$$

where Max and Min represent the decimal maximum and minimum variation across the exit aperture of the integrating sphere, as shown in Figure 2.3.

Radiance calibrations are straightforward when calibrating a single spectral channel in an imaging system. The imager under calibration is first directed toward the integrating sphere such that its field of view is filled by the exit aperture of the integrating sphere. An image is recorded in digital number corresponding to the current radiance of the sphere. The integrating sphere is then varied across several radiance levels, with the imager capturing an image at each radiance. Once this process is complete, the digital number recorded by the imager can be plotted against the known radiance of the sphere for each pixel in each image (Figure 2.4). Once plotted, a linear fit can be performed, creating a relationship between digital number recorded by the imager and radiance (Figure 2.5). The linear fit will take the form

$$y = mx + b, \tag{2.3}$$

where y is the calculated radiance, m is the slope on the linear fit, x is the digital number captured by the imaging system, and b is the intercept of the linear fit. A linear fit can be completed for every pixel on the imager's detector, meaning a unique slope and intercept will be calculated for each pixel. However, as before, hyperspectral data cubes add additional complexities to the calibration process.

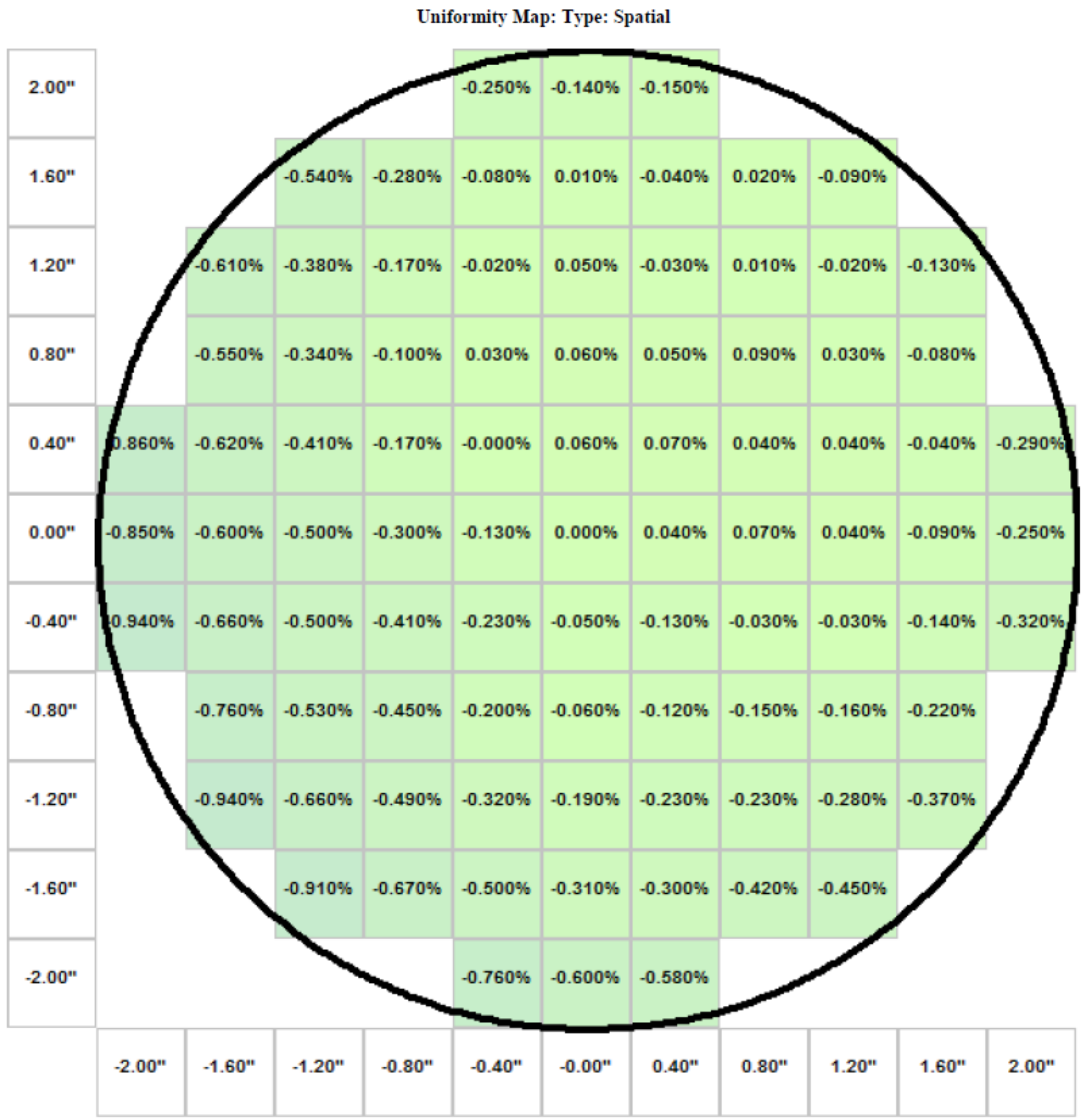

Uniformity	98.97%
Non Uniformity Deviation	0.28%

Figure 2.3: Spatial uniformity across the exit aperture of our Labsphere integrating sphere [19].

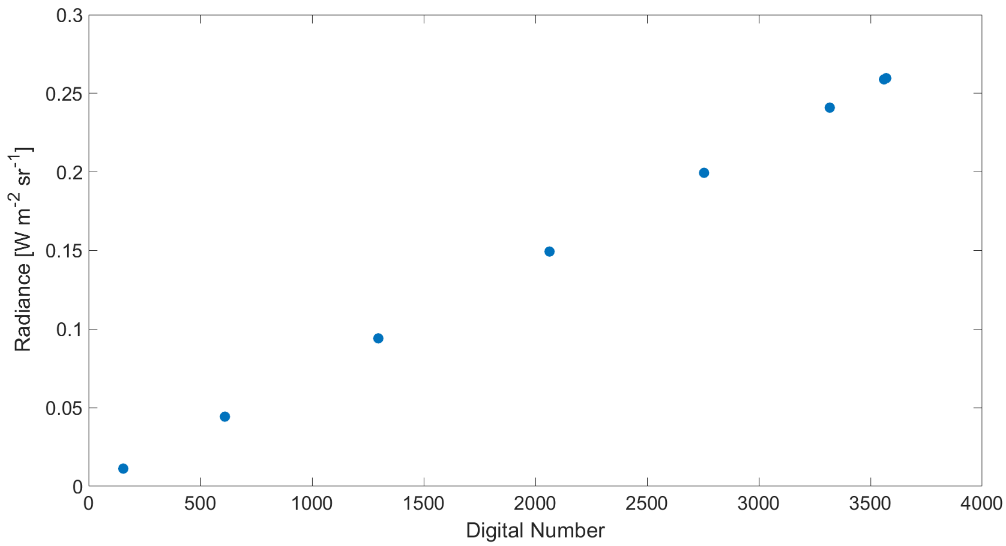

Figure 2.4: Plotting digital number recorded by the imager versus output radiance from integrating sphere.

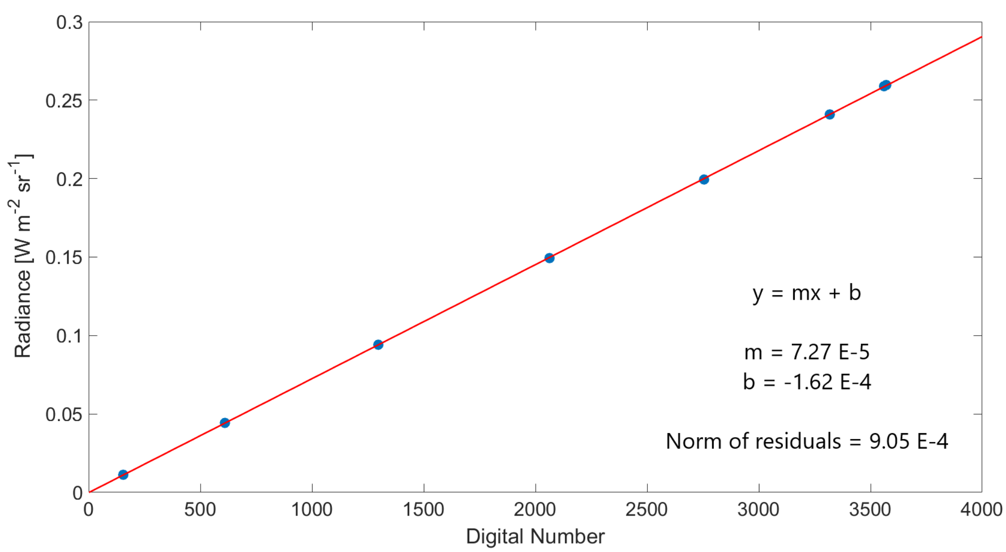

Figure 2.5: Performing a linear fit to obtain a relationship between digital number and radiance. Linear fit statistics shown.

In the example described above, each pixel has a single value and varying the output radiance from the integrating sphere changes that value. When covering the background of hyperspectral imaging, we saw that each spatial pixel in a hyperspectral data cube is represented by a vector comprised of 300 spectral values, representing the spectral channels captured by the imager. This additional complexity means that instead of a single plot of radiance versus digital number for each pixel, a data cube captured by the Pika L requires 300 such plots - one for each spectral channel contained in the pixel. To smooth the spatial uncertainty of the integrating sphere output, we can scan the hyperspectral imager across the center region of the sphere's aperture, gathering 400 frames. If every pixel in the data cube requires calibration across each of its spectral channels, there will be 108×10^6 pixel values for each image. Calibration requires that several radiance values are observed for a linear fit to be obtained, making calibration a computationally expensive process. Therefore, I present two methods for obtaining a radiance calibration with reduced dimensionality: the first involves averaging across one of the spatial dimensions, which I will now refer to as the single-spatial averaging method; the second method averages across both spatial dimensions, which I will refer to as the double-spatial averaging method.

Single-Spatial Averaging Method

A hyperspectral data cube is comprised of two spatial dimensions and one spectral dimension. One spatial dimension is obtained through scanning while the second spatial dimension and the spectral dimension are fixed. If the imager were held stationary and an image captured, the full sensor array would be illuminated and a 900×300 image would be obtained (i.e. 900 spatial pixels and 300 spectral pixels). As the imager is scanned across the scene, this process is repeated and the image frames are stacked together. Due to this image capture process, the spatial dimension obtained by scanning provides redundant information when imaging a uniform scene. To take advantage of this redundancy, while also decreasing random noise in pixel response and smoothing spatial uncertainties in the source, the 400 image frames obtained while capturing the scanned spatial dimension can be averaged, resulting in a 900×300 data cube. Single-spatial averaging reduces the number of data points in each image from 108×10^6 to 270×10^3, reducing the computational expense by a factor of 400.

Double-Spatial Averaging Method

The double-spatial averaging method takes the single-spatial averaging method one step further. After averaging along the scanned spatial dimension, the second spatial dimension is also averaged. Averaging along both spatial dimensions reduces the hyperspectral data cube to a 1×300 vector for each image, reducing the complexity of the data cube by a factor of 360×10^3 from the original image. The result of this process is a 300-element spectrum of gain and a 300-element spectrum of offset for a linear calibration equation of the form of Equation 2.3.

Experimental Setup

All data collected for the radiometric calibration were obtained using our Labsphere integrating sphere as a light source. The Pika L hyperspectral imager was attached to a tripod-mounted rotation stage and directed toward the aperture of the integrating sphere. Images were collected by scanning the Pika L through 400 spatial lines centered on normal incidence with the aperture of the integrating sphere, resulting in a scanned angle of approximately $\pm2^\circ$ about normal incidence. Data cubes were captured at 40 radiance levels, ranging from 192.7 W m^{-2} sr^{-1} to 0.62 W m^{-2} sr^{-1} across a spectral band of 400 nm to 1000 nm.

Results

In this section, I present results obtained by both the single- and double-spatial averaging methods and compare their performance.

Single-Spatial Averaging Method The single-spatial averaging method is meant to decrease the computational expense of analyzing the full hyperspectral data cube; however, this method is still quite data-dense, making it infeasible to use all 40 radiance levels. Additionally, the Pika L exhibits strong linearity across its electronic response, meaning using 40 radiance levels for calibration is unnecessary. For the single-spatial averaging calibration presented here, 5 radiance levels were used. That is, a linear fit was performed using 5 radiance levels on each of the 300 spectral channels for each of the 900 spatial pixels, resulting in 270x10^3 linear fits, mapping digital number to radiance.

To analyze calibration performance, the known spectral radiance output from the integrating sphere (as specified by the manufacturer with a NIST-traceable calibration) was plotted against the calculated spectral radiance obtained through my calibration (Figure 2.6).

Double-Spatial Averaging Method The double-spatial averaging method is meant to further simplify the hyperspectral data cube under analysis to ease computational expense. As this method greatly reduces the dimensionality of the hyperspectral data cubes used for calibration, all 40 radiance levels were used to generate linear fits. That is, 40 data points were computed for each of the 300 spectral channels after double-spatial averaging, resulting in 300 linear fits. The known spectral radiance output of the integrating sphere plotted against the calculated spectral radiance using the double-spatial averaging method is shown in Figure 2.10.

Single-Spatial Versus Double-Spatial Averaging Comparison of the single-spatial and double-spatial averaging methods shows that both methods produce very similar results. The performance of each method is quantified by calculating the percent difference between the calculated and theoretical spectral radiance across all wavelengths (Figures 2.7 and 2.11). I calculated the percent error using the theoretical output of integrating sphere as the accepted value and the calculated spectral radiance as the experimental value. Computing the percent error for the single-spatial averaging method produces 900 values at each spectral channel. That is, a percent error is calculated at each of the spectral channels across all 900 spatial pixels. To present the percent error for the single-spatial averaging method, I averaged the calculated percent error across all 900 spatial pixels to present a single, averaged value for each spectral channel.

To assess the similarity in each method's performance, I subtracted the percent error calculated for each method, revealing that the two methods produce a maximum deviation of approximately 0.26% from one another. Additionally, I calculated the combined uncertainty for each method. To do this, I used the combined relative percent uncertainty reported by the integrating sphere manufacturer along with the percent difference calculated for each method. Then, the uncertainty is calculated as

$$Combined\ Uncertainty = \sqrt{Uncertainty_{sphere}^2 + Uncertainty_{calibration}^2} \tag{2.4}$$

The combined uncertainty in the measurement shows a maximum value of 2.74% and 2.70% for the single-spatial and double-spatial averaging methods, respectively. The maximum uncertainty is found at 400 nm, where sensor responsivity is low.

The similar performance between methods is likely explained by strong uniformity across the aperture of the integrating sphere coupled with low pixel variation on the Pika L imager. The combination of these two factors means that all values recorded by the imager are very similar, such that when averaging is performed, recorded values change very little. However, if both calibration methods were used on a diverse scene, the single-spatial averaging method may outperform the double-spatial averaging method, as it provides a unique and robust calibration spectrum for each pixel in the first spatial dimension. Additionally, systematic error across a scene may be compounded when averaging across all spatial pixels in the double-spatial averaging method. Due to this, the double-spatial averaging should only be used when a calibration is required when computational resources are restricted, such as processing data in the field. Otherwise, the single-spatial averaging method is recommended to provide superior results.

These methods for radiometric calibration are useful for much more than monitoring the ripeness of fruits and vegetables. The Optical Remote Sensor Laboratory may use these radiometric calibrations for many hyperspectral imaging applications. For example, if near real-time radiometric calibrations were required for analyzing hyperspectral images of rivers, the double-spatial averaging method may provide a means of accomplishing that goal. Though the calculation of radiance is useful in many applications, a more informative calibration was used to monitor the ripeness of fruits and vegetables. That is, calculating the spectral reflectance of hyperspectral images provided the most useful information for monitoring ripeness.

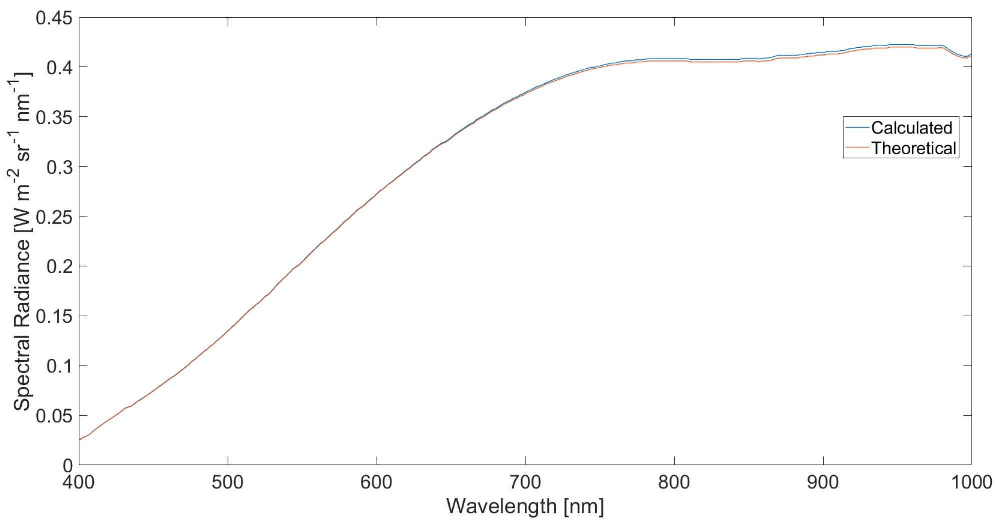

Figure 2.6: Spectral radiance obtained through single-spatial averaging versus theoretical spectral radiance from integrating sphere.

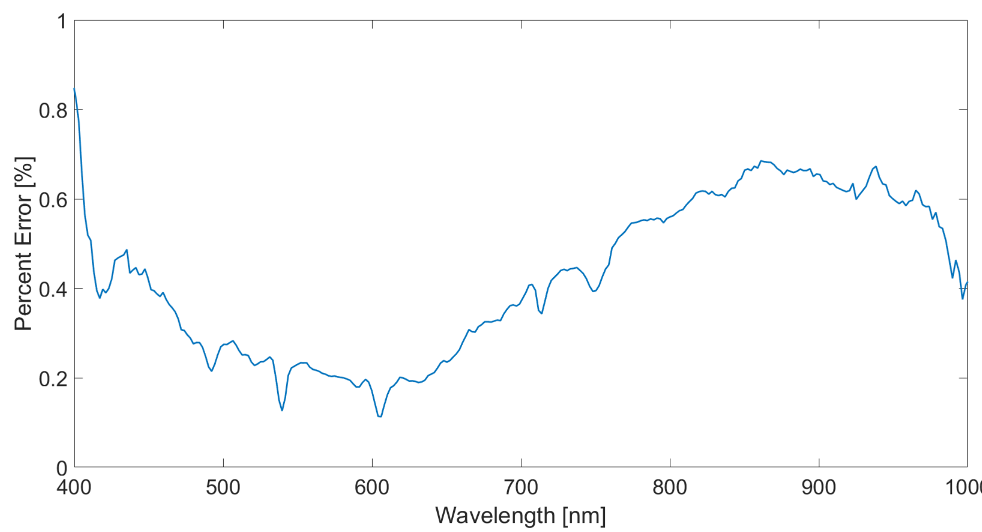

Figure 2.7: Percent difference between theoretical and measured spectral radiance for the single-spatial averaging method.

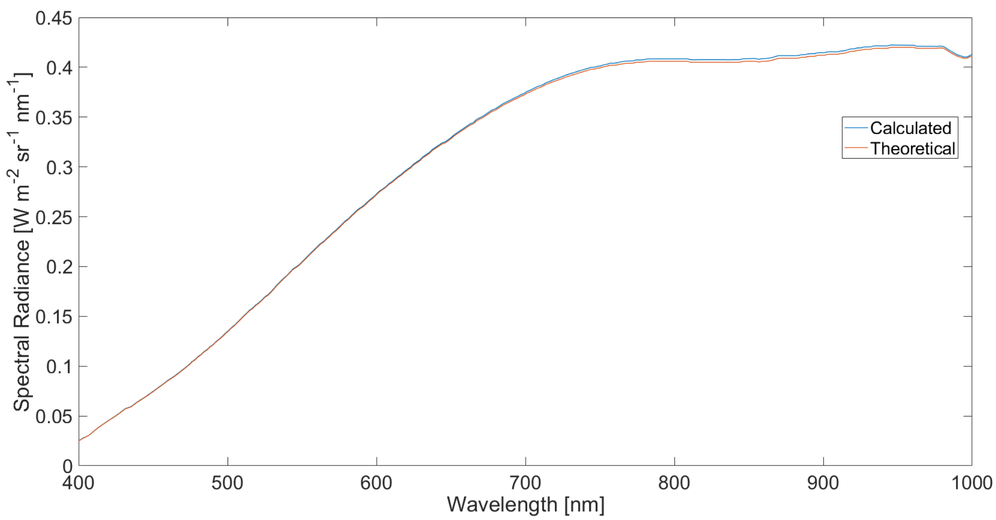

Figure 2.8: Spectral radiance obtained through double-spatial averaging versus theoretical spectral radiance from integrating sphere.

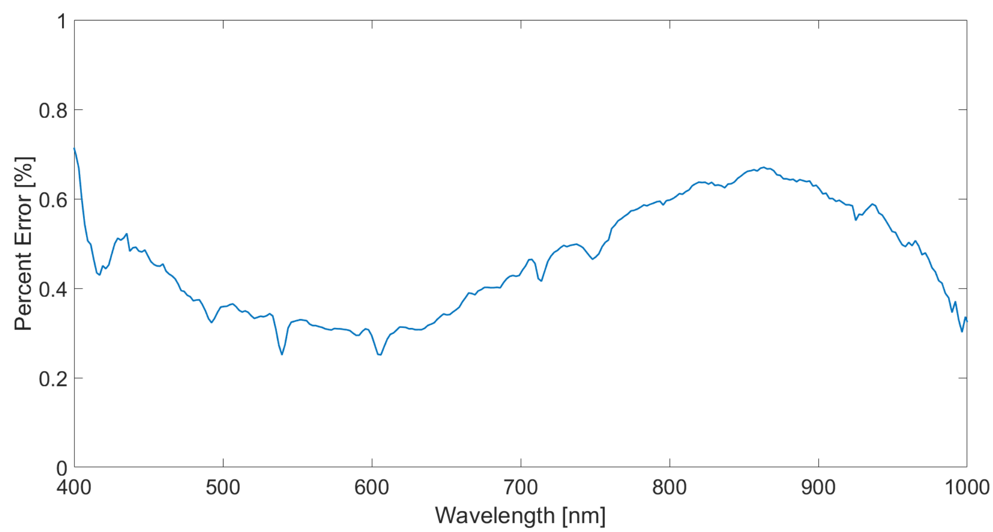

Figure 2.9: Percent difference between theoretical and measured spectral radiance for the double-spatial averaging method.

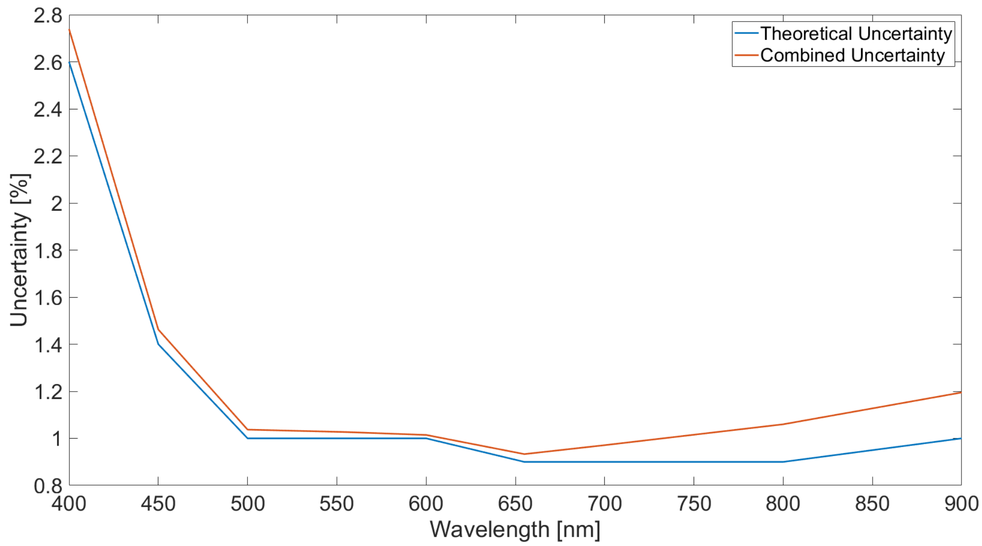

Figure 2.10: Uncertainty in theoretical output of our integrating sphere compared to combined uncertainty for the single-spatial averaging method.

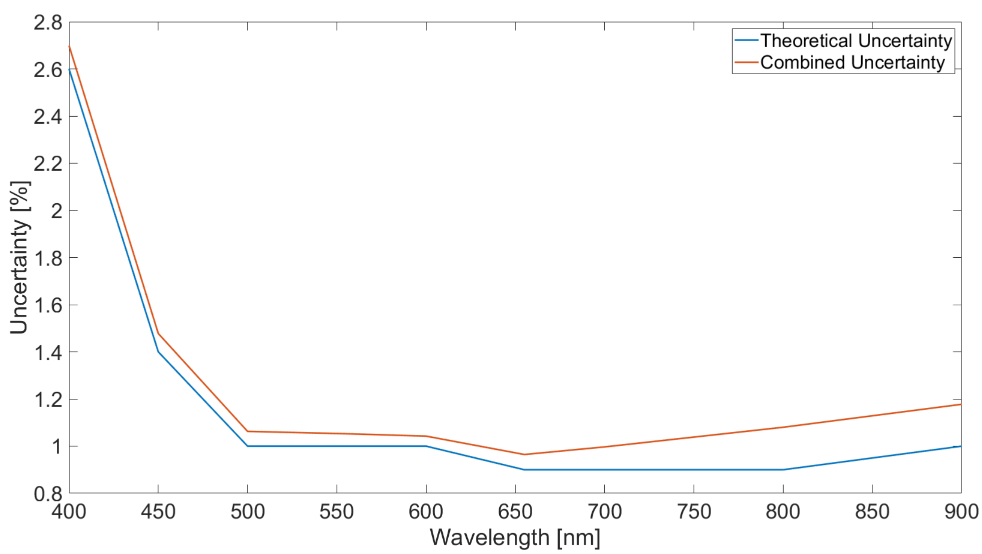

Figure 2.11: Uncertainty in theoretical output of our integrating sphere compared to combined uncertainty for the double-spatial averaging method.

Calculation of Reflectance

Reflectance is defined as the ratio of incident light reflected off a surface to the total light incident on that surface. This calculation is commonly performed by using a reflectance target, or a piece of material that approximates a Lambertian surface and has known reflectance across a certain portion of the electromagnetic spectrum. By using this known reference, all points in the image can be compared to the value recorded on the target and quantified between 0 and 1, where 1 represents 100% of the incident light being reflected off the surface. Mathematically, reflectance is calculated as

$$\rho = \left(\frac{DN_{scene} - DN_{dark}}{DN_{target} - DN_{dark}} \right) \rho_{target}, \tag{2.5}$$

where the reflectance, ρ, is calculated from an imaging system capturing units of digital numbers (DN) from the scene and from the panel of reflectivity ρ_{target}. DN_{dark} represents the dark current, or background signal generated through sporadic electron generation in the imager's sensor.

Reflectance offers many advantages over the raw digital numbers recorded by an imaging system. Specifically, calculating reflectance removes any wavelength-dependent response of the imaging system and provides robust results across varying lighting conditions.

The first advantage, the removal of any wavelength-dependent response, is a benefit of the normalization inherent in calculating reflectance. As reflectance is a ratio of two values, both captured by the same imager, any unique digital or optical response in the imager is automatically canceled through the calculation.

The second advantage, the ability to provide results across varying lighting conditions, relies on several factors: (1) the reference target must be illuminated by the same light source as the broader scene being imaged, (2) the target must be placed at the same angle as the objects in the scene (i.e. if imaging an object lying flat on the ground, the reference target cannot be tilted), and (3) if the reference target is contained within the scene, it must be at approximately the same distance as the objects being analyzed. Ideally, the reliance on these factors is mitigated by capturing an image while filling the field of view of the imaging system with a large reflectance target illuminated by the same light source and placed at the same distance and angle as the objects being imaged. Doing so allows for the reflectance to be calculated at a pixel-by-pixel basis. However, the experimental design employed in this work did not allow for the test produce to be moved, so the use of a large reflectance panel was not feasible. Instead, we placed two smaller Spectralon panels within the image. These panels, along with a general pipeline of calculating reflectance is shown in Figure 2.12.

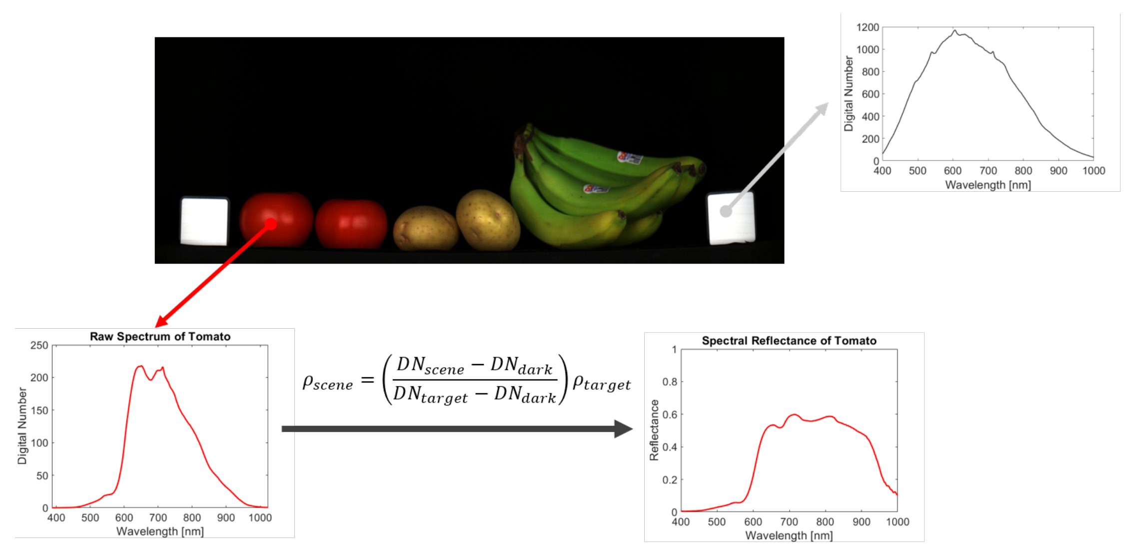

Figure 2.12: Example of calculating reflectance for a single pixel containing information from a tomato.

First, the raw digital number spectrum is chosen from a single pixel in the image, providing values for DN_{scene}. The digital number spectrum recorded on the reflectance target provides a value for DN_{target}. The known reflectivity of the reflectance target provides a value for ρ_{target} ranging from 0 to 1, where 1 represents 100% reflectivity. Carrying out the calculation of reflectance at this pixel results in the reflectance spectrum shown.

The placement of two Spectralon panels within the image provided a convenient means of calculating the reflectance spectrum as the test produce aged without having to adjust the setup. However, if the pixel-by-pixel response of the imager had significant differences, the pixels containing the reflectance panels could not be used to calibrate the pixels containing the other objects in the scene. Therefore, the pixel uniformity of the Pika L had to be tested.

Pixel Uniformity

To measure the uniformity of pixel response across the Pika L's detector array, I imaged the spatially uniform output of the integrating sphere by scanning the imager across the sphere's aperture. As each of the line-scans captured across the aperture of the integrating sphere responds with the same pixels on the imager's detector, averaging pixel values across the scanned spatial dimension results in a 900 spatial pixel $\times$ 300 spectral pixel image, similar to the single-spatial averaging method outlined during the radiometric calibration. Since the integrating sphere does not have uniform spectral radiance emittance between 400 nm to 1000 nm, each of the spectral channels captured by the Pika L have a unique response. To report the spatial uniformity, the non-uniformity deviation metric is calculated as

$$Non\text{-}Uniformity\ Deviation = \frac{Standard\ Deviation}{Mean} \tag{2.6}$$

for all spatial pixels at each spectral channel.

Using 36 images of the spatially uniform output of the integrating sphere, I calculated the mean and standard deviation of the 900 spatial pixels for each image across 6 spectral channels. From the resulting 36 means and standards deviations for each spectral channel, I calculated the average value of both the mean and standard deviation. Table 2.2 shows the spatial non-uniformity deviation across all measured spectral channels, with maximum values of 2.67% before application of the radiometric calibration and 0.33% after radiometric calibration, compared to the known integrating sphere spatial uniformity of approximately 1% as reported by the integrating sphere manufacturer. Additionally, before each image capture, I subtracted the dark signal from each image using the SpectrononPro software.

Table 2.2 shows that the Pika L has very low pixel non-uniformity, especially after performing a radiometric calibration. These results provide a justification for using reflectance targets that are only present in a portion of an image to calibrate all pixels in the image. In the context of this work, the non-uniformity deviation results justify the use of two Spectralon panels contained on the edges of the imagery. As additional justification, since the physical layout of the experiment remains the same throughout the measurement cycle, the panels are imaged on the same pixels under the same lighting conditions. Therefore, even if a small error is introduced by using different pixels for produce and reflectance panel measurements, that error only manifests itself as a small systematic reflectance offset. However, this introduces another question when obtaining daily measurements: how stable is the imager

Table 2.2: Spatial non-uniformity deviation of the Pika L hyperspectral imager.

Wavelength [nm]	Uncalibrated Non-Uniformity Deviation [%]	Calibrated Non-Uniformity Deviation [%]
449.6	1.49	0.15
550.0	1.42	0.11
650.3	1.52	0.11
750.4	1.62	0.11
850.2	2.03	0.16
949.6	2.67	0.33

response between image captures?

Image Stability Analysis

Monitoring the ripeness of fruits and vegetables requires comparing imagery collected daily to assess spectral changes as a function of time. To ensure the digital response of the Pika L was stable enough to make this comparison, I performed an image stability analysis. This analysis was performed by capturing 15 consecutive images in a dark lab with a cap covering the objective lens of the Pika L. The temporal stability of the Pika L can be assessed by calculating the mean and standard deviation of the digital numbers recorded throughout image capture (Figure 2.13). The maximum calculated standard deviation was 0.253 out of a maximum response of 39 digital numbers, resulting in a maximum deviation of approximately 0.6% between images. The low variation between images justifies the experimental methodology

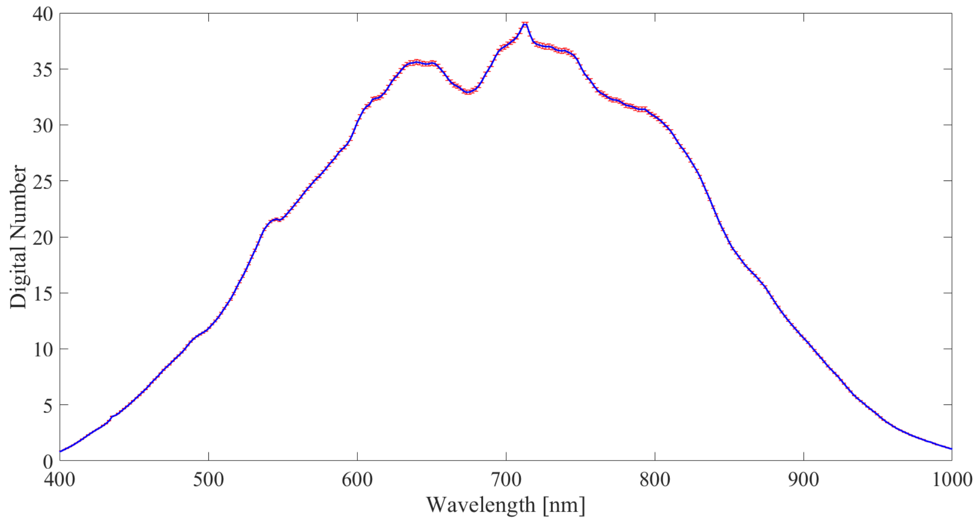

Figure 2.13: Mean (blue) and standard deviation error bars (red) after taking 15 consecutive dark images with the Pika L.

of comparing images captured daily, as spectral content in the images will not be substantially affected by image stability. Though the spectral content is minimally affected by imager stability, the accuracy of the spectral information captured by the Pika L had to be analyzed.

Spectral Characterization

The aging process of produce is associated with a change in spectral content. However, to accurately use spectral content as a metric to quantify aging in produce, the spectral performance of the Pika L needed to be characterized. For example, if a particular pigment present in bananas absorbed 680 nm, I needed to ensure that the Pika L recorded this absorption feature at the correct wavelength. To perform this characterization, I swept a monochromator (Acton Research Corporation SpectraPro-150) across 400 nm to 1000 nm in steps of 10 nm, outputting light with a spectral resolution of 0.4 nm. At each step, I captured a hyperspectral data cube and

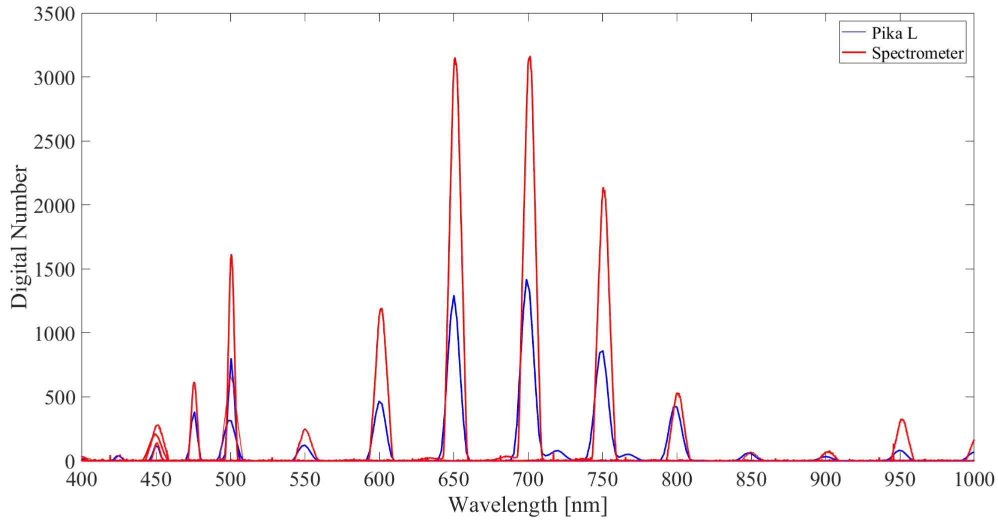

Figure 2.14: Spectral bands captured by the Pika L (blue) and the Ocean Optics spectrometer (red). Band centers of monochromator output shown on the x-axis.

spectrometer (Ocean Optics USB4000-VIS-NIR) measurement which has a spectral resolution of approximately 1.5 nm full width at half maximum (FWHM). Using both the monochromator and spectrometer provided a two-point verification of the performance of the Pika L. The spectral bands captured by the Pika L and the spectrometer are shown in Figure 2.14.

For simplification, the captured bands are shown for monochromator outputs in steps of 50 nm, as listed on the x-axis. Peak values measured by the Pika L and spectrometer fell within 2.12 nm of each other and the band center of the monochromator output, confirming good spectral accuracy. Measurements at 500 nm and below show four measurements due to second order diffraction from the internal grating in the monochromator. To confirm absolute accuracy in future characterizations, I plan to obtain hyperspectral data cubes of reflected helium-neon (HeNe) laser light or atomic lamps. After confirming good spectral accuracy across the spectral range of the Pika L, a broadband illumination source for the test produce was required.

Illumination Source Analysis

Halogen-tungsten bulbs are a common illumination source of broadband light (Figure 2.15). These lamps produce light when an electrical current flows through a tungsten filament surrounding by halogen gas. However, as the tungsten filament warms, its resistance changes, leading to a change in brightness. To measure the time until the warm-up period ends and the brightness reaches a steady state, I used a broad-spectral range spectrometer (ASD FieldSpec Pro) capturing information across a spectral range of 350 nm to 2500 nm. Using the spectrometer, I measured the output of our halogen-tungsten lights until the signal recorded by the spectrometer remained constant for multiple readings.

The wavelength showing the most significant change (737 nm) shows the change in brightness as a function of time (Figure 2.16). Though the halogen-tungsten lamps do require roughly 7 minutes to reach a steady state, the change in brightness is quite small, with a change of approximately 0.31% throughout the warm-up process.

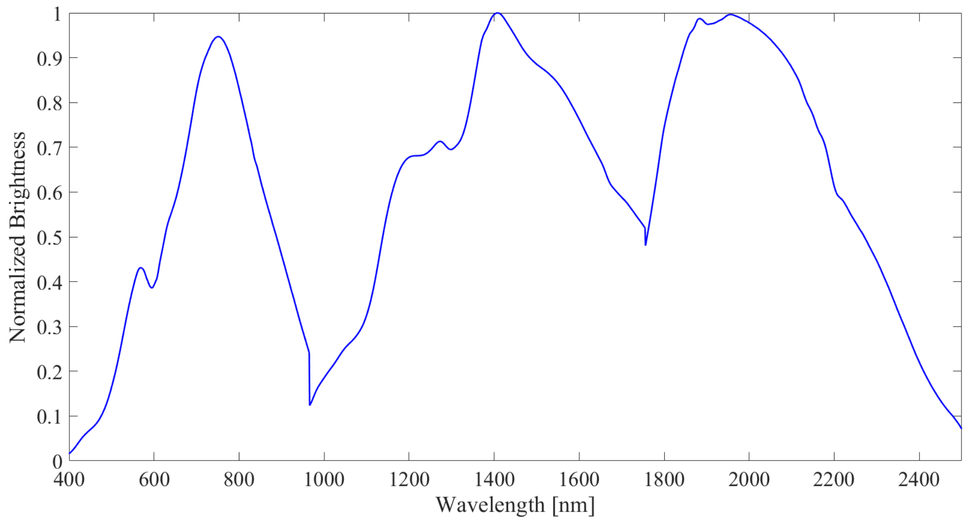

Figure 2.15: Uncalibrated spectral output from a halogen-tungsten lamp measured with 3-detector spectrometer, resulting in the 3 response peaks shown.

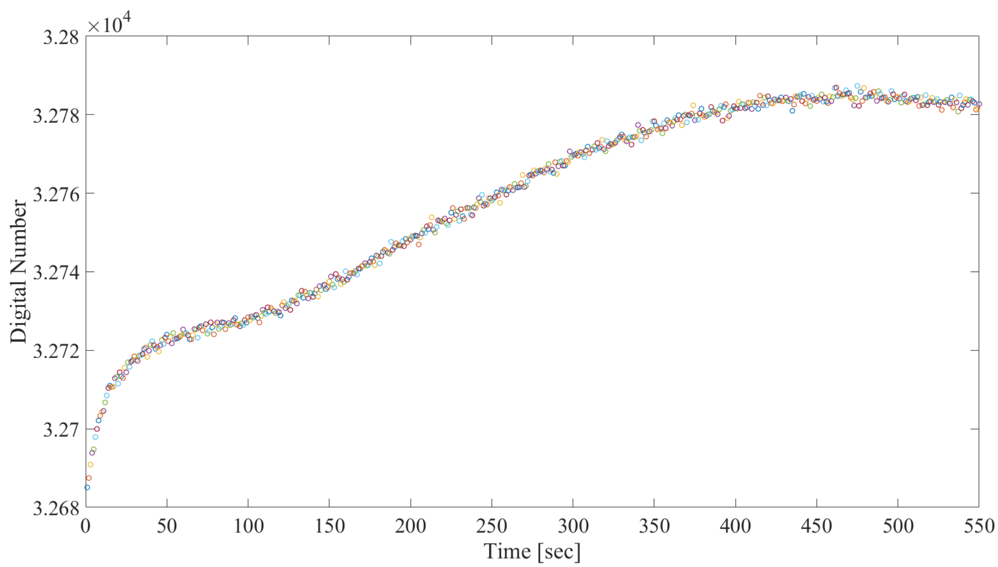

Figure 2.16: Spectral output of our halogen-tungsten lamp as a function of time at 737 nm.

MEASURING THE POLARIZATION RESPONSE OF A VNIR HYPERSPECTRAL IMAGER

Contribution of Authors and Co-Authors

Author: Riley D. Logan

Contributions: Performed experiments and analyzed results.

Author: Joseph A. Shaw

Contributions: Provided funding and technical guidance for measurements and analyses.

Manuscript Information

Riley D. Logan and Joseph A. Shaw

SPIE Proceedings Volume 11412, Polarization: Measurement, Analysis, and Remote Sensing XIV; 114120K (2020)

Status of Manuscript:
____ Prepared for submission to a peer-reviewed journal
____ Officially submitted to a peer-reviewed journal
____ Accepted by a peer-reviewed journal
____ Published in a peer-reviewed journal
_X_ Published in conference proceedings

SPIE
1 April 2020
27 April 2020
doi: 10.1117/12.2558257

Though the Pika L imager was not designed for polarization imaging, many hyperspectral imaging systems are partially sensitive to polarization [41]. As many scenes commonly contain partially polarized light, ignoring the polarization-sensitivity of a system may lead to erroneous results. In the context of observing fruits and vegetables, light can become partially polarized when reflected from the glossy surface of produce.

To create the variable linear polarization states used to determine the polarization response of the Pika L system, I used an integrating sphere and a large-aperture polarizer mounted in a rotation stage. This produced a spatially uniform source of linearly polarized light with a user-selected orientation. The test polarizer was a 108–mm-diameter (129-mm-diameter when mounted) wire-grid polarizer with an extinction ratio of at least 1000 between 400 nm to 1000 nm (Meadowlark Optics VLM-129-UV-C). I directed the Pika L, attached to a tripod-mounted rotation stage, to view the polarized light transmitted through the wire-grid polarizer from the integrating sphere by sweeping it through a small angular range of approximately 2° centered on normal incidence, resulting in a maximum angle of incidence of $\pm 1^\circ$ on the polarizer (Fig. 3.1). Using the Resonon SpectrononPro software package, I set the Pika L to capture 200 lines with a frame rate of 40 Hz, an integration time of 21 ms, and a gain of 0.

To avoid stray light from entering the system, I baffled the path between the polarizer and imager, then shrouded the entire experimental setup as an additional precaution. Beginning with a vertical orientation, I rotated the polarizer clockwise (when looking into the polarizer and integrating sphere) through 180° in steps of 2°. At each step, I collected three hyperspectral data cubes and averaged to reduce noise. Using the averaged data cubes, I converted units from digital number to radiance to account for the wavelength-dependent response of the imaging system. This was done

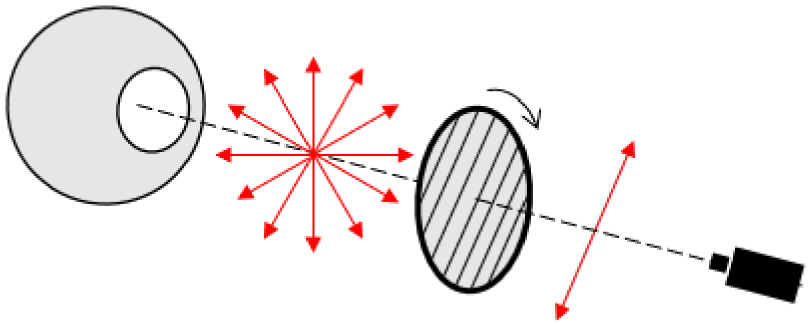

(a)

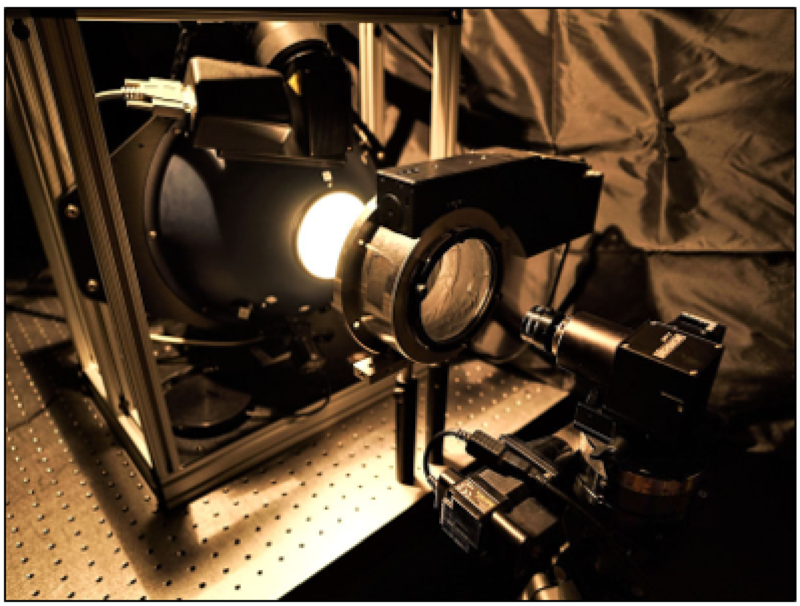

(b)

Figure 3.1: Experimental setup (a) and physical setup showing the integrating sphere, wire-grid linear polarizer, and Pika L imager without baffling in place (b).

using a previous radiometric calibration derived by relating measured digital numbers to the variable integrating sphere radiance with no polarizer or other elements in the optical path. Once the data were converted into radiometric units, I calculated the polarization response spectrum of the Pika L from the change in spectral radiance as a function of polarizer angle. To further quantify the polarization response of the Pika

L, I calculated the apparent S_0, S_1, and S_2 Stokes parameters and the apparent degree of linear polarization (DoLP) that indicates the instrument's polarization-dependent relative spectral response function.

The Pika L shows a clear dependence on the polarization state of incoming light, especially in the near-infrared spectral range beyond 700 nm wavelength. To visualize the polarization-dependent response of the imaging system, I plotted the spectra measured at 90 different polarizer angles, along with the fixed source output spectrum after passing through the test polarizer, as defined by the integrating sphere calibration certificate after multiplication by the polarizer's typical spectral transmittance curve (Fig. 3.2). Each colored line in the spread of measured spectral radiance represents a different polarization state. The red line depicts the theoretical radiance curve output by the integrating sphere, with its internal aperture 90% open, after passing through the test polarizer. I attribute the difference between the theoretical source spectral radiance and measured source spectral radiance to deviations from typical reported performance in our test polarizer, resulting in additional loss factors that extend beyond spectral transmittance effects. The loss factors could potentially be accounted for if a radiometric calibration were completed with the test polarizer in place, but this was not done for the measurements reported here.

Closer inspection of one wavelength with low polarization response (614 nm) and four wavelengths with strong polarization response (682 nm, 744 nm, 828 nm, 958 nm) helps to illuminate the dependence on polarizer angle (Fig. 3.3a-e). I plotted each of the selected wavelengths as a function of polarizer angle and normalized to the decimal fraction of the S_0 Stokes parameter. If the Pika L had no polarization response, or a wavelength with little polarization-dependence were observed, the imager would be expected to record $S_0/2$ across all polarizer angles, as given by Malus's Law (Fig.

3.3a). However, Figures 3.3b-e actually show a maximum variation of approximately $\pm 3.7\%$ about $S_0/2$.

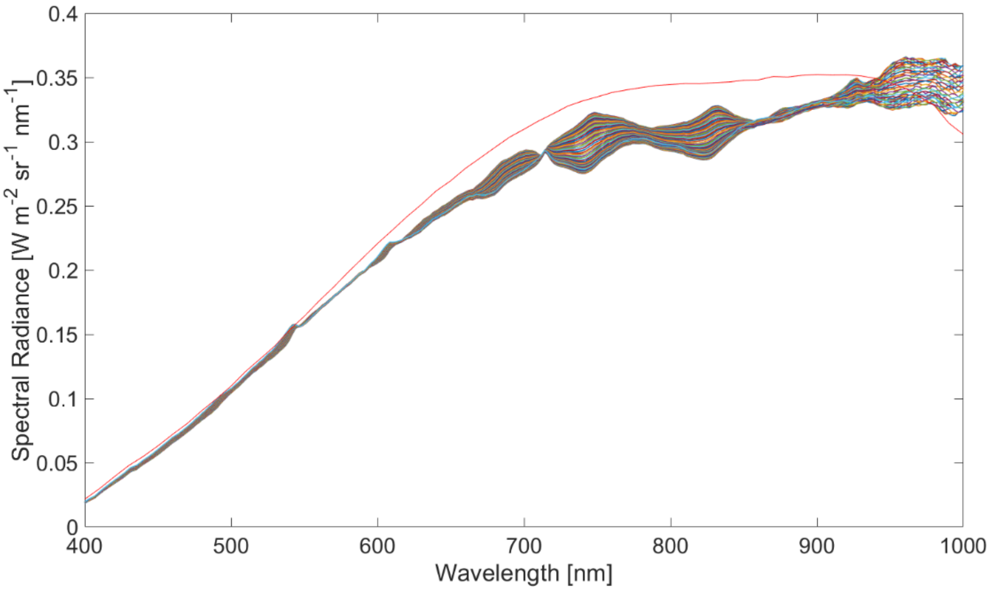

Figure 3.2: Integrating sphere output spectral radiance (red) and source spectral radiance measured by the Pika L at different polarizer angles (multi-color).

To better visualize the polarization response of the imager, we calculated the apparent degree of linear polarization (DoLP). To perform this calculation, we defined the S_0, S_1, and S_2 Stokes parameters as

$$S_0 = L_{0^\circ} + L_{90^\circ} \tag{3.1}$$

$$S_1 = L_{0^\circ} - L_{90^\circ} \tag{3.2}$$

$$S_2 = L_{45^\circ} - L_{135^\circ}, \tag{3.3}$$

with L_{0°, L_{90°, L_{45°, and L_{135° representing the detected spectral radiance for vertically, horizontally, 45°, and 135° polarized light, respectively.

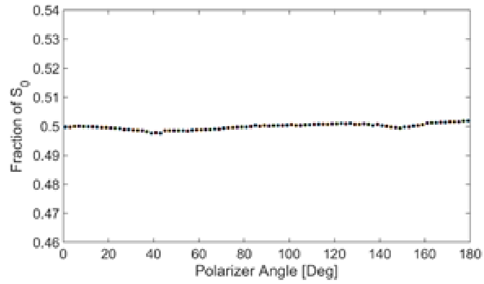

(a) 614 nm

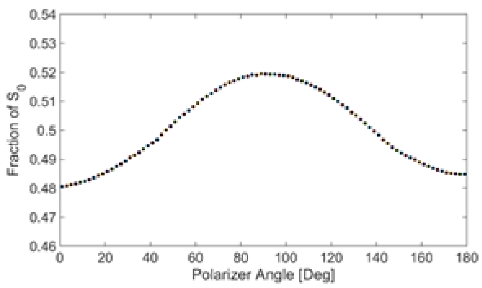

(b) 682 nm

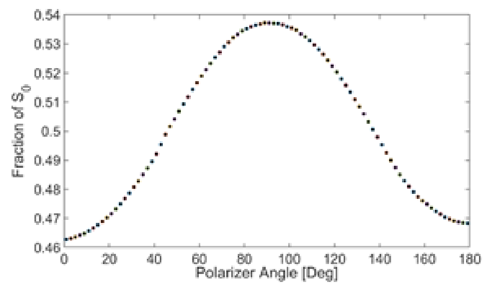

(c) 744 nm

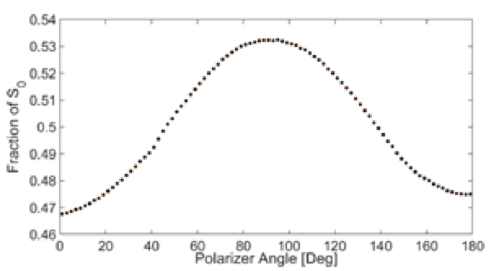

(d) 828 nm

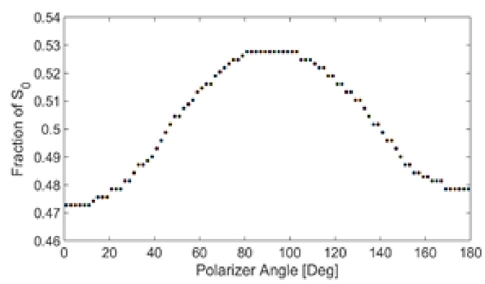

(e) 958 nm

Figure 3.3: Polarization response of the Pika L in terms of S_0 as a function of polarizer angle at selected wavelengths.

Using these three Stokes parameters, I calculated the DoLP, which expresses the fraction of the light that is linearly polarized, as

$$DoLP = \frac{\sqrt{S_1^2 + S_2^2}}{S_0}. \tag{3.4}$$

Usually, the DoLP represents the decimal fraction of an incident electromagnetic wave that is linearly polarized, but here I am using the DoLP to quantify the amount of variation in the measurement of completely polarized light introduced by polarizer angle. In other words, I am using the DoLP to quantify the amount by which the measured signal extends above and below $S_0/2$ as a function of polarizer angle for each wavelength. To visualize this quantity, I calculated the DoLP across all measured wavelengths for the Pika L imager (Fig. 3.4). As depicted in Figure 3.4, the Pika L imager has a polarization response that depends strongly on wavelength. The DoLP varies between a minimum value of approximately 0.001 (0.1%) at 614 nm to a maximum value of 0.073 (7.3%) at 744 nm.

The results from this polarization response analysis are ongoing. Currently, efforts are being made to model and compensate for the polarization response observed. Compensating for this polarization response will allow for more accurate hyperspectral images for any scene containing partially polarized light. For example, if obtaining imagery for river ecology studies, correcting for the partially polarized light reflected from the surface of the water will lead to more accurate data products.

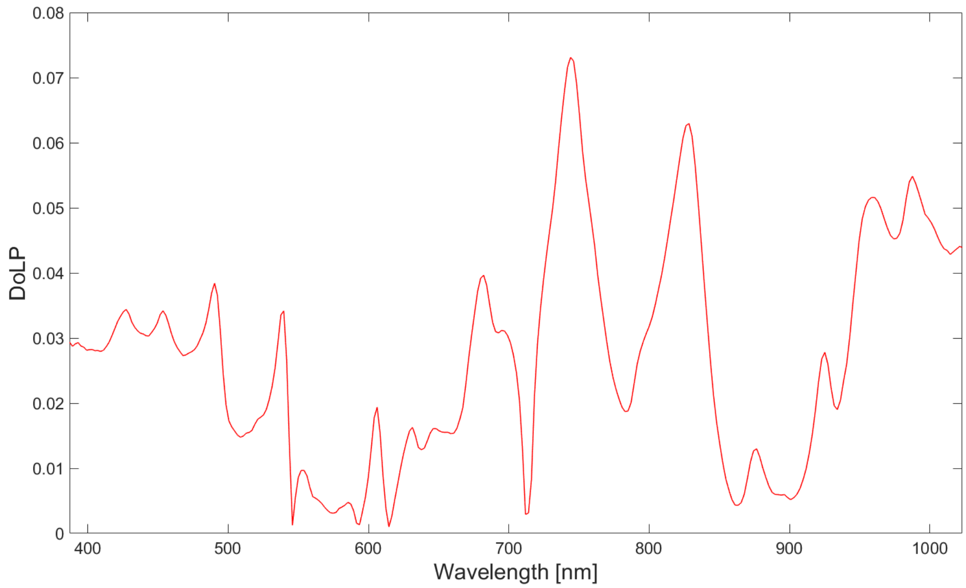

Figure 3.4: Degree of linear polarization as a function of wavelength for the Pika L imager.

HYPERSPECTRAL IMAGING AND MACHINE LEARNING FOR MONITORING PRODUCE RIPENESS

Contribution of Authors and Co-Authors

Author: Riley D. Logan

Contributions: Calibrated the Pika L hyperspectral imaging system, designed the experiment setup, captured image data to be provided to computer scientists for analysis with machine learning algorithms, helped computer science students understand and work with hyperspectral imagery.

Author: Bryan Scherrer

Contributions: Aided in hyperspectral image analysis.

Author: Jacob Senecal

Contributions: Developed machine learning algorithms for analysis of various fruits and vegetables tested, including a convolutional neural network capable of determing age of produce.

Author: Neil S. Walton

Contributions: Developed machine learning algorithms for analysis of various fruits and vegetables tested, including a genetic algorithm capable of determining salient wavelengths from a hyperspectral data cubes.

Author: Amy Peerlinck

Contributions: Aided in the development machine learning algorithms for analysis of various fruits and vegetables tested.

Author: John W. Sheppard

Contributions: Provided funding and technical guidance for machine learning algorithm development and analysis.

Author: Joseph A. Shaw

Contributions: Provided funding and technical guidance for optical measurements and analysis.

Manuscript Information

Riley D. Logan, Bryan Scherrer, Jacob Senecal, Neil S. Walton, Amy Peerlinck, John W. Sheppard, and Joseph A. Shaw

SPIE Proceedings Volume 11421, Sensing for Agriculture and Food Quality and Safety XII; 114210O (2020)

Status of Manuscript:
____ Prepared for submission to a peer-reviewed journal
____ Officially submitted to a peer-reviewed journal
____ Accepted by a peer-reviewed journal
____ Published in a peer-reviewed journal
__X__ Published in conference proceedings

SPIE
13 April 2020
27 April 2020
doi: 10.1117/12.2560968

Produce Measurement Methodology

After characterizing and calibrating the Pika L hyperspectral imager, it could be used to gather meaningful data. In this chapter, I discuss the application of the calibration and characterization of the imager for the analysis of fruits and vegetables. First, I introduce an overview of our experimental procedure, beginning with a broad overview of our processing steps. I then discuss the imaging system and light sources used to gather image data, the experimental setup and testing procedure, image preprocessing, and final processing steps.

Experimental Procedure

The experimental procedure used throughout this work is illustrated as a flowchart in Fig. 4.1. This processing flowchart will serve as a road map of our experimental methods, beginning with our imaging system and illumination techniques.

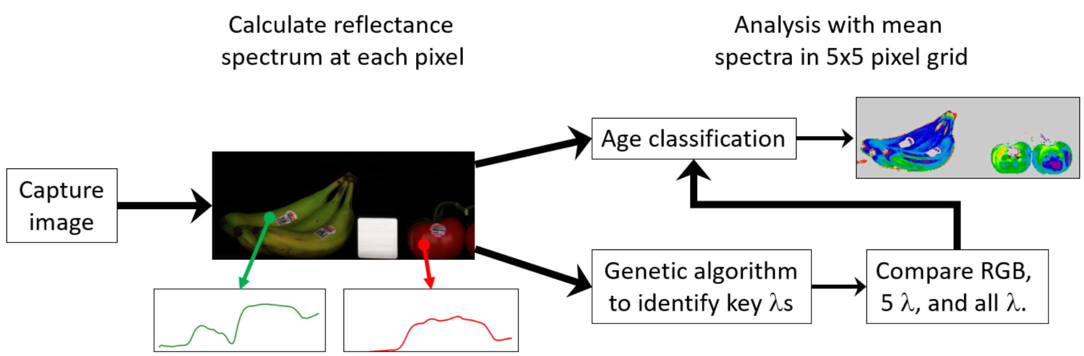

Figure 4.1: Process flowchart used to outline our experimental methods.

Imaging System and Light Sources

All image data were collected using a Resonon, Inc. visible near-infrared (VNIR) Pika L hyperspectral imaging system across a spectral range of 387.12 nm to 1023.50 nm with a spectral resolution of approximately 2.12 nm, producing 12-bit hyperspectral data cubes with 300 spectral channels. We performed a radiometric calibration on our Pika L imager, assessed its polarization response, validated its spectral and pixel-to-pixel performance, and analyzed its image-to-image stability.

Light Sources Not all light sources produce light over the Pika L imager's spectral range of 400 nm to 1000 nm. For example, fluorescent and LED lighting commonly found in grocery stores provides only a small portion of this spectrum. To alleviate this issue for laboratory studies, we illuminated our samples with two 500 watt tungsten-halogen bulbs mounted behind diffusing screens. Each source was positioned at $\pm$ 30° from the imaging axis, resulting in approximately uniform illumination of the test samples (Fig. 4.2). We converted the raw digital numbers captured by the imaging system to reflectance by placing two 5 cm x 5 cm, 99% reflective Spectralon reference plates (Labsphere SRT-99-020) next to the produce. Further detail are discussed in Sec. 4.

Experimental Setup and Testing Procedure

Measurements were made with produce sitting on a specially designed low-reflectance produce stage, alongside the two reflectance calibration targets, and scanning the imager through a full angle of approximately 24° (Fig. 4.3). We maintained consistent camera settings throughout the measurement cycle, with a gain of 1, frame rate of 30 fps, and exposure time of 10 ms using the SpectrononPro software provided by Resonon, Inc.. The low-reflectance produce stage kept stray

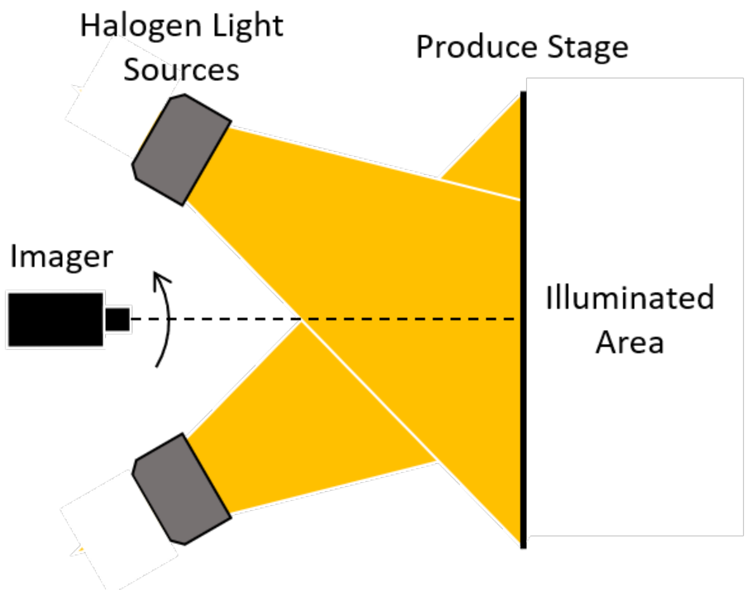

Figure 4.2: Overview of experimental setup showing halogen light orientation, imager position and scanning direction, and illuminated stage on which produce and reflectance targets were placed.

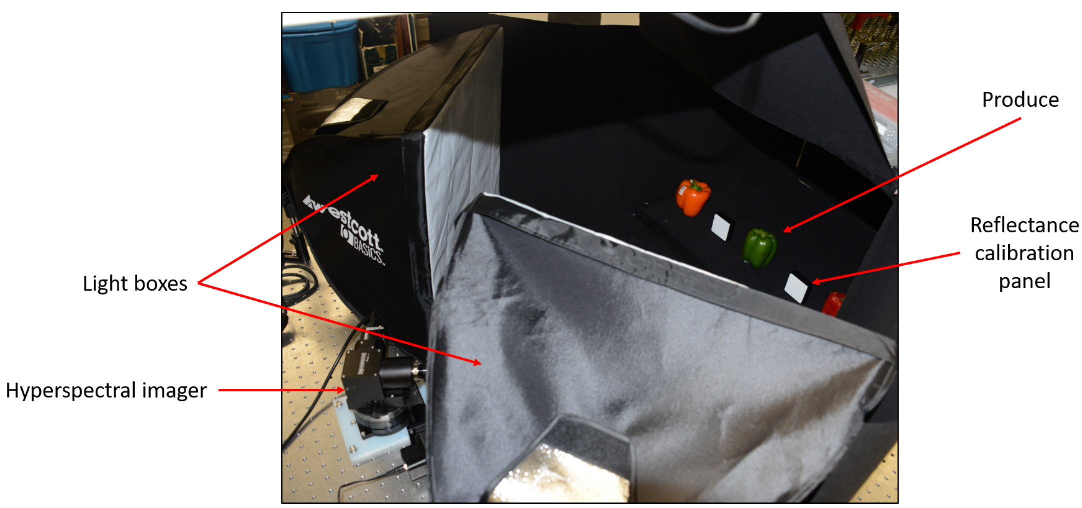

Figure 4.3: Experimental setup in practice, showing light sources, hyperspectral imager, produce stage, test produce, and reflectance panels.

light from entering the test stage while also reducing multiple reflections between the walls of the produce stage and other pieces of produce or other objects in the setup.

We began with fresh produce obtained from a local grocery store and ended each measurement when the produce was visibly inedible (i.e. rot or mold present). Store employees informed us that produce was restocked from distribution vehicles every 1-3 days, meaning fresh test produce was easy to obtain. We selected test samples from the most commonly available items in produce departments. In this paper, we discuss measurements of bananas, bell peppers, avocados, Yukon Gold potatoes, and tomatoes. We chose test produce by selecting the least-ripe options readily available on grocery store displays, judging by appearance, texture, firmness, shape, and smell. Once purchased, we placed the test produce on the produce stage in our temperature-controlled laboratory, held at an average ambient temperature of 21.7°C and average relative humidity of 27.5%, throughout the course of our measurements. Once positioned on the produce stage, the test produce was not allowed to shift position until the ripening process was complete. By not moving the samples, we obtained measurements of the same area on the test produce throughout the entire observation period. To maximize data collection, we placed multiple pieces of test produce in the produce stage and collected samples from each piece of visible produce in the stage. Data were collected for over a year, with the number of days of aging data for each piece of produce shown in Table 4.1. However, many days of data collection contained multiple samples of an individual piece of produce and many regions on each piece of produce were used for analysis.

Preprocessing

The preprocessing pipeline used in this work contains removing the dark signal from the hyperspectral data cube, converting the data cube to reflectance, and

Table 4.1: Days of aging data collected for each type of produce presented.

Produce	Days of Aging Data
Bananas	64
Yukon Gold Potatoes	60
Green Bell Peppers	47
Avocados	77
Tomatoes	87

isolating produce pixels in each data cube. To begin, we covered the objective lens of the imager using a lens cap and captured a dark image. After subtracting the mean digital number obtained from the dark image, the raw data cube was converted to reflectance, found as the ratio of signals from the produce pixel signals and the Spectralon pixels, as outlined in Chapter 2. This calculation was performed at each spatial location, giving us a reflectance spectrum from 400 nm to 1000 nm at each spatial location in the imaged scene (Fig. 2.12).

In the final preprocessing step, we manually identified and isolated the test produce in each data cube. By isolating the test produce, we created a training set for our classification and age analysis algorithms discussed in Sec. 4.

Processing

In this section, I discuss the development of machine learning algorithms to classify the type of produce under analysis, the relative age of the test produce measured from the time of purchase, and for selecting the most informative wavelengths for use in a low-cost multi-spectral imager.

Age Analysis The main part of the analysis performed here was with respect to determining the age of the produce that had been imaged. For this step, we employed a convolutional neural network architecture that we call "SpectrumNet." The details of this network are described in Senecal [38], with a specific description of its application to related multispectral classification problems in Senecal *et al.*[39]

The basic architecture of SpectrumNet defines a set of "spectral" modules that correspond to squeeze layers and expand layers. The squeeze layers define the bulk of the network, except for a convolutional layer placed at the beginning and end of the network. In addition, depthwise convolution and batch normalization are incorporated into the squeeze and expand layers, thereby significantly reducing the computational burden of the network. The resulting network consisted of an input layer, a convolutional layer, three spectral layers (combining squeeze and expand), a max-pooling layer, six more spectral layers, a final convolutional layer, and an average pooling layer. A basic feedforward prediction layer was then placed on the top with classes corresponding to *fresh* and *non-fresh*.

Wavelength Selection Given that our goal is to deploy a low-cost imager in a grocery store setting, it is evident that full hyperspectral imaging is unlikely to be cost-effective. As a result, we have been investigating alternative methods for selecting small subsets of wavelengths from the spectrum for purposes of designing low-cost, multi-spectral imagers tailored to the produced being monitored. With this in mind, we developed a method using a genetic algorithm (GA) that simultaneously selects a subset of informative wavelengths and identifies effective filter bandwidths for such an imager.

Our approach involves fitting a multivariate Gaussian mixture model to a histogram of the GA population at convergence, selecting the wavelengths associated with the peaks of the distributions as our solution. Using this method, we are also able to specify filter bandwidths by calculating the standard deviations of the Gaussian distributions and computing the full-width at half-maximum values. In our experiments, we find that this novel histogram-based method for feature selection is effective when compared to both the standard GA and partial least squares discriminant analysis. Details on this approach can be found in Walton *et al.*[45] and Walton.[44]

Produce Measurement Results

In this section, I discuss the results obtained for the analysis of bananas, tomatoes, avocados, Yukon Gold potatoes, and bell peppers. I begin with an overview of the reflectance image data obtained throughout the measurement process then move to a discussion of the performance of the machine learning algorithms developed for classification, age analysis, and wavelength selection. Finally, I discuss the possible implementation of our methodology into a grocery store setting.

All reflectance data presented in this section represent a single piece of produce as it ages. I hand-selected a small section of the produce and analyzed it each day using the Spectralon analysis software. Careful selection of the piece of produce ensured that the same region on the piece of test produce was analyzed each day. To convert image data to units of reflectance, I hand-selected a uniform region of a Spectralon panel in each image, avoiding the edges of the panel where spatial uniformity appears to decrease. The presented reflectance spectra represent that portion of the piece of produce as it ages across the time scale shown. An example of selecting a region for analysis on a banana and claibration region on a reflectance panel is shown in Figure 4.4. The mean and standard deviation across the reflectance panel is also shown, with a maximum standard deviation of approximately 2.7%.

Image Analysis of Bananas, Tomatoes, Avocados, Yukon Gold Potatoes, and Bell Peppers

Changes in the chemical makeup of produce during ripening (e.g. decreasing chlorophyll content) result in changes in the reflectance spectrum [20, 30, 34, 40]. This process is illustrated for a banana in Fig. 4.5. When a banana is in the early stages of ripening, high chlorophyll content gives it a characteristic green color [21]

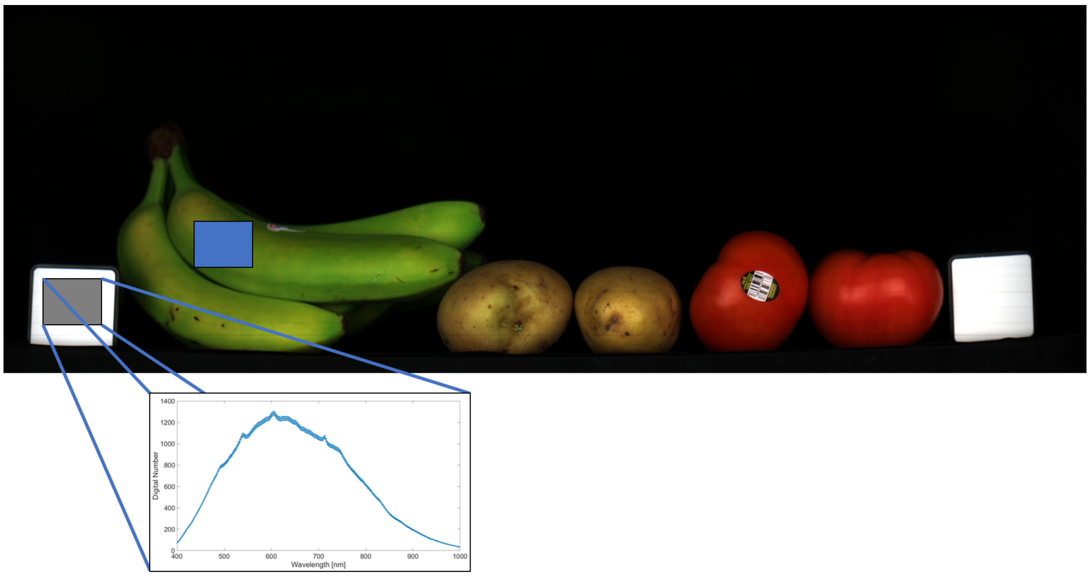

Figure 4.4: Example of selecting an analysis region on a banana (blue square) and calibration region on a reflectance panel (gray square). Mean and standard deviation across the panel's surface is shown.

(Fig. 4.6a). The chlorophyll absorption is evident as the large trough near 680 nm in the reflectance spectrum. As the banana ripened and chlorophyll content decreased, the visible color of the banana shifted from green to yellow (Fig. 4.6b). This phase of ripening is represented in Days 3 - 7, during which the chlorophyll absorption trough decreased and spectral features between approximately 550 nm to 900 nm became smoother. When the banana was browning and becoming soft at the end of its ripeness cycle (Fig. 4.6c), the spectral reflectance features were almost entirely smooth (days 9 - 11).

The reflectance spectra of other types of produce also change systematically during the ripening process. For example, though selecting a ripe avocado is can be a bewildering task for some shoppers, our measurements of avocados showed relatively direct aging activity (Fig. 4.7). Avocado ripening is a complex process, with water

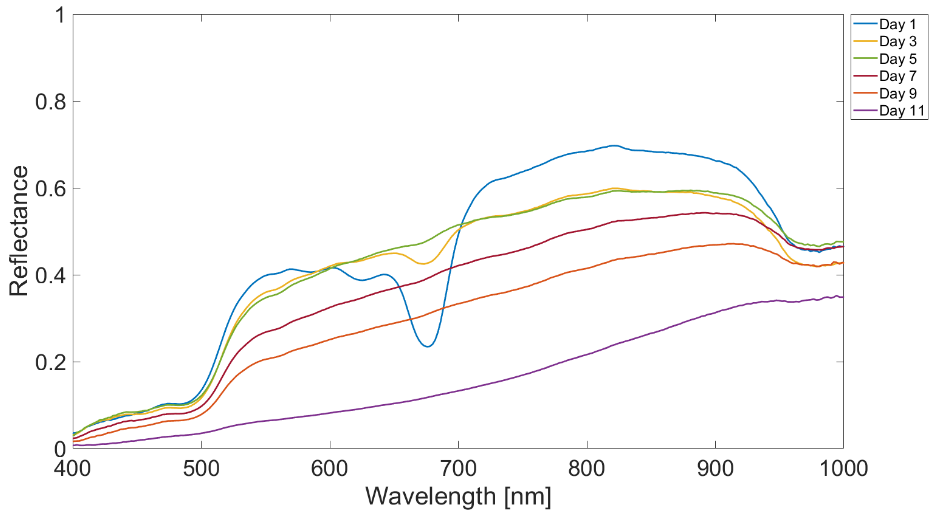

Figure 4.5: Temporal variation in the spectral reflectance of a banana. Each line represents a measurement of the same banana taken on different days.

(a) Day 1 (b) Day 5 (c) Day 11

Figure 4.6: RGB images of the ripening process of bananas across 11 days.

content, ethylene content, and temperature all playing a role [2]. When not yet ripe, the avocado took on a firm, green appearance, represented by the increased reflectance near 550 nm and high reflectance at the knee of the red edge just beyond 700 nm (days 1 - 3). As the avocado ripened, its skin became darker and its reflectance decreased significantly beyond 700 nm (days 5 - 11). When the avocado became too ripe too eat and shriveling occurred because of decreased in water content, the reflectance remained below 10% until approximately 800 nm, where an increase in reflectance occurred (days 13 - 19).

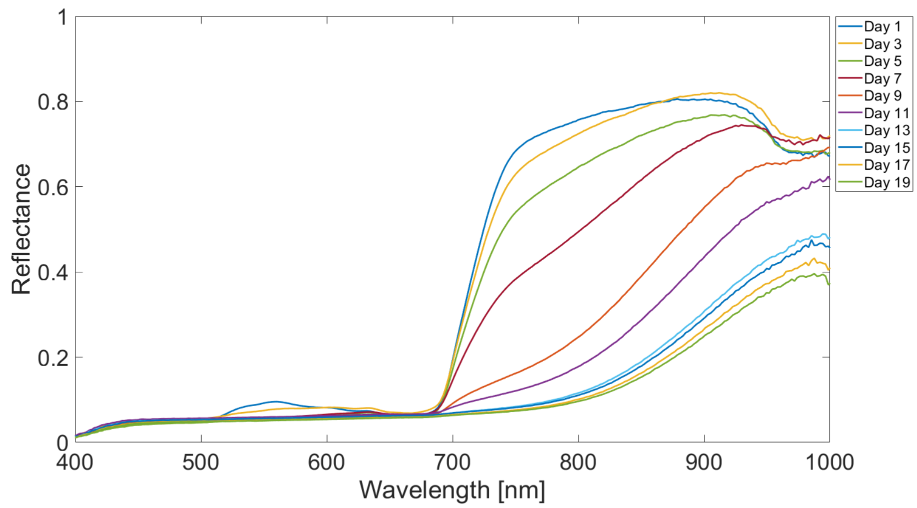

Figure 4.7: Temporal variation in the spectral reflectance of avocados. Each colored curve represents a new measurement day on the same avocado.

Though bananas and avocados exhibit clear ripening processes, not all test produce we analyzed followed this theme. To expand our analysis of produce commonly available at grocery stores, we analyzed green, yellow, orange, and red bell peppers. Freshly purchased bell peppers exhibited a unique spectral curve for each color (Fig. 4.8). Though unique spectral curves are helpful for classification, they create a challenge for determining consistent measures for aging across all varieties of peppers. An additional challenge was considering the temporal variation in the reflectance spectra of peppers. Despite the unique spectrum for each pepper color, which arises because of both chlorophyll and carotenoids that have observable absorption features in our spectral range [25], our measurements showed there is no simple change in the spectral reflectance as the pepper ages (Fig. 4.9). Though there may be some detectable change in the relative heights of the two large reflectance peaks or the slope of the reflectance ramp from approximately 600 nm to 700 nm, often denoted as the red edge, the ripening process in peppers is much more difficult to detect.

Tomatoes present a similar challenge. Tomato ripening is characterized by varying lycopene content in the skin, the breakdown of chlorophyll, and the build-up of carotenes [32]. Though absorption features for chlorophyll and lycopene are well-known, our measurements showed no clear temporal variation of the reflectance spectra as the tomato aged (Fig. 4.10). While the tomato was still fresh, there was some indication of a chlorophyll absorption feature near 680 nm, but this feature was subtle and only present during very early stages of the ripening process.

The final piece of produce presented in this section is the Yukon Gold potato. When potatoes are exposed to incident light for an extended period, an increase in chlorophyll production occurs in a process known as greening [12]. Greening is undesirable due to its adverse effect on potato marketability and the development of the toxic group of plant compounds, glycoalkaloids. The greening process was evident when observing the reflectance spectra of a Yukon Gold potato over the course of 17 days (Fig. 4.11). As the potato aged and chlorophyll production increased, an absorption feature developed near 680 nm. It is interesting to note that this aging process is nearly opposite of bananas, with a chlorophyll absorption feature developing as the potato aged.

To explore the detection and use of the spectral features outlined above, we turned to machine learning algorithms. We began by developing a genetic algorithm to identify salient wavelengths in the image data. That is, the genetic algorithm was used to choose a number of wavelength which carried the most information for classifying the age of the produce under test. Next, we developed a convolutional

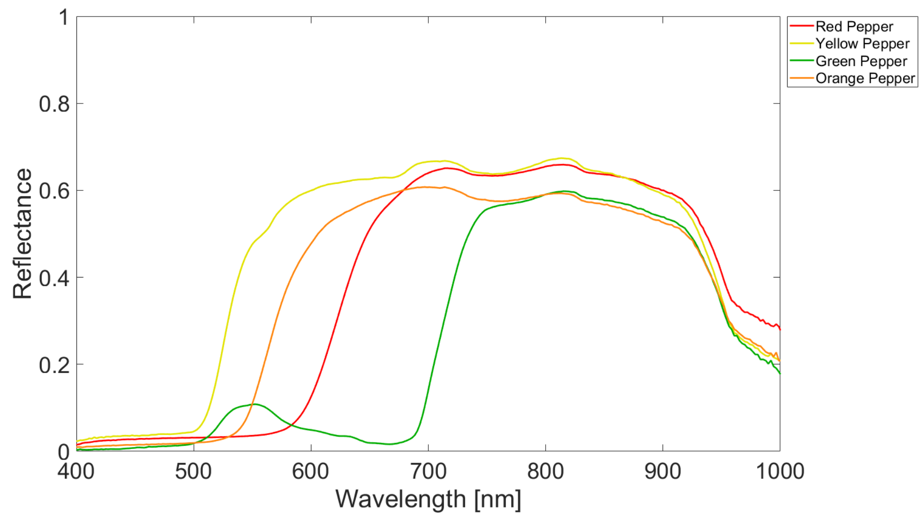

Figure 4.8: Variation in the spectral reflectance of bell peppers. Each colored curve represents a different variety of bell pepper.

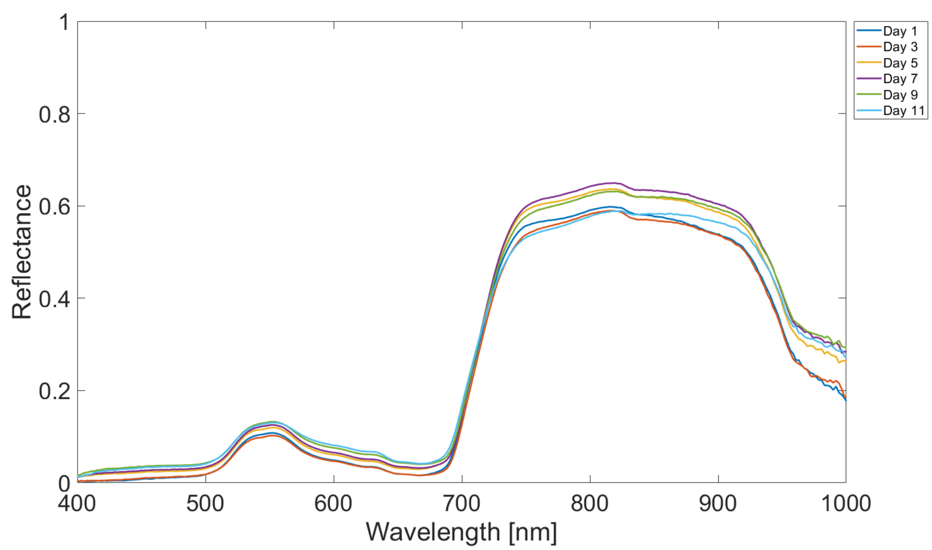

Figure 4.9: Temporal variation in the spectral reflectance of a green bell pepper. Each line represents a measurement of the same pepper taken on different days.

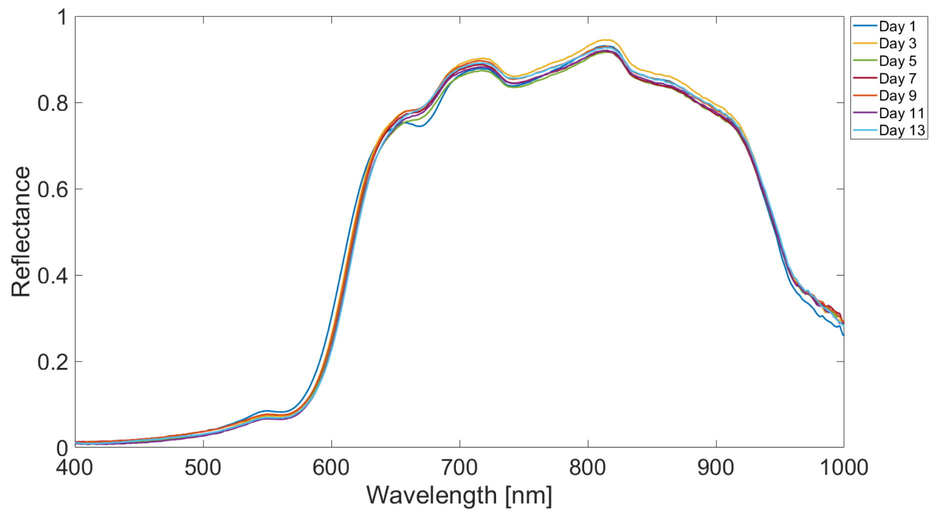

Figure 4.10: Temporal variation in the spectral reflectance of a tomato. Each line represents a measurement of the same tomato taken on different days.

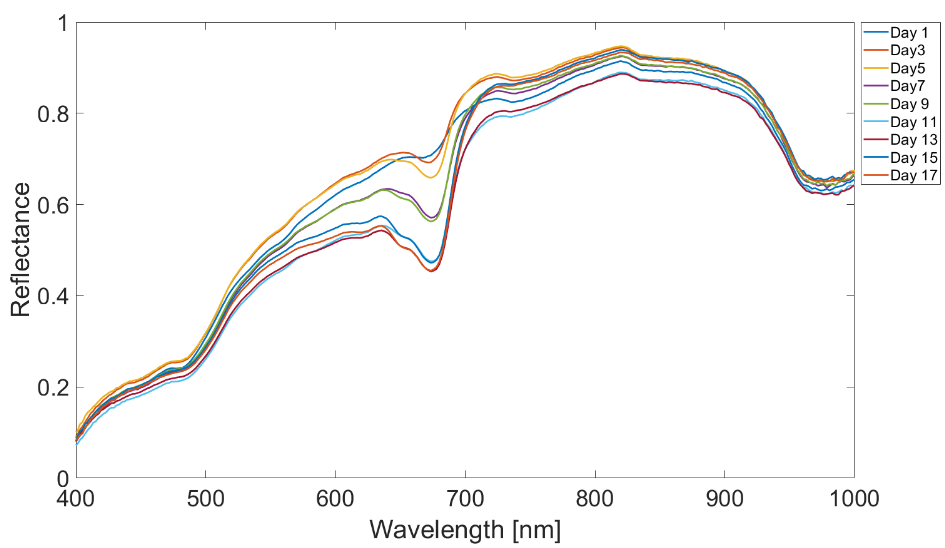

Figure 4.11: Temporal variation in the spectral reflectance of a Yukon Gold potato. Each line represents a measurement of the same potato taken on different days.

neural network to perform the age classification. The age classification was performed across three produce sets, including bananas, Yukon Gold potatoes, and green peppers. We compared the age classification performance of the convolutional neural network for three wavelengths sets: RGB wavelengths, the full hyperspectral spectrum, and the wavelengths selected by the genetic algorithm. Complete details of the methodology and results of these analyses are reported elsewhere [23].

CONCLUSION

Food waste around the world is becoming increasingly problematic, with over one billion metric tons recorded in 2011 [15, 43]. In the United States alone, 113 million metric tons of food were wasted in 2010, meaning that approximately 29% percent of the food produced for human consumption went to waste. This wasted food results in an economic cost of between 165$ and 198$ billion annually in the U.S. [13, 43], emission of harmful greenhouse gasses [16, 26], the consumption of one-quarter of freshwater resources, and nearly 300 million barrels of oil [16]. In this work, I presented a method for using hyperspectral imaging and machine learning to help decrease food wasted by monitoring the ripeness of fruits and vegetables in grocery stores.

Hyperspectral imaging provides information-dense images by capturing hundreds of contiguous spectral channels from a scene. The spectral channels captured in a hyperspectral imager can be used to monitor the optical properties of objects in the scene. The optical properties of an object determine the amount of light absorbed, transmitted, or reflected from an object. In the case of fruits and vegetables, optical properties are largely driven by the chemical makeup of the produce under analysis. For example, levels of the common pigment, chlorophyll, change in many fruits and vegetables throughout the ripening cycle. The change in the chemical makeup of produce can be observed through the reflectance spectra obtained through hyperspectral imaging. However, imaging systems must be calibrated before the data contained in the captured imagery can be analyzed.

The calibration and characterization methods I presented in this work go well beyond the analysis of fruits and vegetables, with useful information for applications such as precision agriculture and river ecology studies. In this work, the Resonon

Pika L hyperspectral imager [35], was characterized and calibrated.

The first calibration I performed, the radiometric calibration, provided a means of converting the raw digital numbers captured by the imaging system to scientific units of radiance. This unit conversion is accomplished by capturing images of a light source at various, known radiance levels, then performing a linear regression between the raw digital numbers captured by the imager and the known radiance of the source. For the Pika L, I proposed two methods of performing this calibration: The single-spatial averaging method, in which all pixels are averaged along the scanned spatial dimension, then a linear fit is performed on the remaining 900 spatial pixels across all 300 spectral channels. The double-spatial averaging method in which the data cube obtained after the single-spatial averaging is further simplified by averaging along the remaining 900 spatial pixels, resulting in a 1×300 vector. A linear fit is obtained for all 300 spectral channels remaining in the vector. Both averaging methods obtained good results, with deviations from the known spectral output from the integrating sphere less than 0.68%. Interestingly, the performance from each calibration method was nearly identical, implying the output of the integrating sphere is highly uniform and high pixel uniformity of the Pika L.

The next characterization I presented discussed converting from the raw digital numbers captured by the Pika L to reflectance. This calculation is performed by using reflectance targets in the image. The Spectralon reflectance targets used in this work diffusely reflected approximately 99% of the incident light, provided a reference to calculate the reflectance of the other objects in the image. Reflectance is advantageous as it corrects for any wavelength-dependent response of the imaging system and is robust across varying lighting conditions.

To use small reflectance panels to calculate reflectance for the entire image meant I needed to ensure the Pika L exhibited strong pixel uniformity. To test this metric, I calculated the non-uniformity deviation across all pixels at six different wavelengths before and after radiometric calibration. The pixel non-uniformity showed a maximum value of 2.67% before calibration and 0.33% after calibration.

Along with pixel uniformity, I needed to test the image stability of the Pika L. To accomplish this, I captured 15 consecutive dark images and compared the digital number values from each image. The Pika L showed high stability with a maximum deviation of 0.6% between images.

As the Pika L relies on detecting hundreds of spectral channels, I analyzed the spectral accuracy of the imager. To do this, I swept a monochromator across the spectral range of the Pika L and captured a hyperspectral data cube every 10 nm. I compared the spectral band captured by the Pika L to a spectrometer measurement and the reported output from the monochromator. As values agreed within 2.12 nm, showing good spectral accuracy.

To provide information at all of the spectral channels captured by the Pika L, I used halogen-tungsten lights. However, these light sources also required analysis due to the heating of the tungsten filament. I analyzed the warm-up time of the lamps by measuring their spectral output using a spectrometer until the lamp output reached a steady state. From this analysis, I found the warm-up time to be approximately 7 minutes with a maximum change of roughly 0.31% at 737 nm.

Though the Pika L is not a polarimetric instrument, the Optical Remote Sensor Laboratory commonly uses it to capture images that may contain partially polarized light. Partial polarization in a scene may arise from reflections from the surface of water or from the glossy surface of fruits and vegetables. To determine how the Pika L responded to different polarization states of light, I imaged the output of an integrating sphere, held at a constant radiance, through a wire-grid polarizer. To control the polarization state of the imaged light, I rotated the wire-grid polarizer in steps of 2°through 180°and captured an image at each step. The maximum degree of linear polarization was found to be approximately 7.3% at 744 nm.

Using these calibrations and characterizations, the Pika L could be reliably used to monitor the ripeness of fruits and vegetables as a part of a larger research team including computer scientists, electrical engineers, and optical scientists [24]. Once calibrated, hyperspectral data cubes were obtained with produce placed in a specially designed, low-reflectance stage. Measurements were made once a day throughout the life cycle of the produce being tested, which included bananas, tomatoes, potatoes, avocados, and bell peppers. For analysis, all measurements were converted into reflectance spectra using two Spectralon panels placed on the produce stage.

Using the reflectance spectra, machine learning algorithms were used to analyze the ripeness of fruits and vegetables. Age analysis experiments were performed with a novel convolutional neural network. Experiments were run using both RGB images and hyperspectral images to compare performance. Feature selection was performed using a genetic algorithm (GA). Using the GA, we selected salient wavelengths from the full hyperspectral spectrum and compared age classification performance against RGB images and hyperspectral imagery. Preliminary data from these analyses show promising results.

The GA-based feature selection method presented provides a method for determining salient wavelengths for a given application. Currently, this method is being used to develop and test a low-cost multispectral imager for use in age classification of bell peppers.

For future work, further efforts in development and testing of a wide range of multispectral imagers for age classification of produce in grocery stores could be explored. Along with using the GA-based feature selection method to help develop low-cost multispectral imagers, we hope to use the calibrations presented in this work to aid in the analysis of the applications the Pika L is employed for, such as precision agriculture and river ecology studies.

REFERENCES CITED

[1] Judith A Abbott. Quality measurement of fruits and vegetables. *Postharvest Biology and Technology*, 15:207–225, 1999.

[2] J P Bower and J G Cutting. Avocado fruit development and ripening physiology. Technical report, 1988.

[3] Jean C Buzby, Hodan F Wells, and Jeffrey Hyman. The Estimated Amount, Value, and Calories of Postharvest Food Losses at the Retail and Consumer Levels in the United States. *USDA-ERS Economic Information Bulletin*, (121), 2014.

[4] Wilson Castro, Jimy Oblitas, Miguel De-La-Torre, Carlos Cotrina, Karen Bazan, and Himer Avila-George. Classification of cape gooseberry fruit according to its level of ripeness using machine learning techniques and different color spaces. *IEEE Access*, 7:27389–27400, 2019.

[5] Sergio Cubero, Nuria Aleixos, Enrique Molto, Juan Gomez-Sanchis, and Jose Blasco. Advances in machine vision applications for automatic inspection and quality evaluation of fruits and vegetables. *Food Bioprocess Technology*, 4:487–504, 2011.

[6] EdmundOptics. Optical Glass, 2020.

[7] Nashwa El-Bendary, Esraa El Hariri, Aboul Ella Hassanien, and Amr Badr. Using machine learning techniques for evaluating tomato ripeness. *Expert Systems with Applications*, 42(4):1892 – 1905, 2015.

[8] Esraa Elhariri, Nashwa El-Bendary, Ahmed M. M. Hussein, Aboul Ella Hassanien, and Amr Badr. Bell pepper ripeness classification based on support vector machinedetecting rottenness caused by pennicillium genus fungi in citrus fruits using machine learning techniques. *ICET 2014 - 2nd International Conference on Engineering and Technology*, 2014.

[9] Frida Femling, Adam Olsson, and Fernando Alonso-Fernandez. Fruit and vegetable identification using machine learning for retail applications, 2018.

[10] FOSCO. PIN Photodetector Characteristics for Optical Fiber Communication – Fosco Connect.

[11] Juan Gomez-Sanchis, Jose D. Martin-Guerrero, Emilio Soria-Olivas, Marcelino Martinez-Sober, Rafael Magdalena-Benedito, and Jose Blasco. Detecting rottenness caused by pennicillium genus fungi in citrus fruits using machine learning techniques. *Expert Systems with Applications*, 39(1):780–785, 2012.

[12] Laura Grunenfelder, Larry K. Hiller, and N. Richard Knowles. Color indices for the assessment of chlorophyll development and greening of fresh market potatoes. *Postharvest Biology and Technology*, 40(1):73–81, apr 2006.

[13] Dana Gunders. Wasted: How America Is Losing Up to 40 Percent of Its Food from Farm to Fork to Landfill. *NRDC Issue Papers*, (12-06-B), 2012.

[14] Otkrist Gupta, Anshuman J. Das, Joshua Hellerstein, and Ramesh Raskar. Machine learning approaches for large scale classification of produce. *Scientific Reports*, 8(1), 2019.

[15] Jenny Gustavsson, Christel Cederberg, Ulf Sonesson, Robert Van Otterdijk, and Alexandre Meybeck. Global Food Losses and Food Waste - Extent, causes and prevention. In *International Congress Save Food!*, Rome, 2011. Food and Agriculture Organization of the United Nations.

[16] Kevin D. Hall, Juen Guo, Michael Dore, and Carson C. Chow. The Progressive Increase of Food Waste in America and Its Environmental Impact. *PLoS ONE*, 4(11):e7940, nov 2009.

[17] M S Kim, Y R Chen, and P M Mehl. Hyperspectral Reflectance and Fluorescence Imaging System for Food Quality and Safety. *Transactions of the ASAE*, 44(3):721–729, 2001.

[18] Labsphere. Integrating Sphere Theory and Applications. Technical report, Labsphere, 2017.

[19] Labsphere. Uniformity Mapping Test Report. Technical report, 2018.

[20] Danielle Laval-Martin, Joélle Quennemet, and René Monéger. Pigment Evolution in Lycopersicon Esculentum Fruits During Growth and Ripening. *Phytochemistry*, 14(11):2357–2362, 1975.

[21] Meng Li, David C. Slaughter, and James F. Thompson. Optical chlorophyll sensing system for banana ripening. *Postharvest Biology and Technology*, 12(3):273–283, dec 1997.

[22] Haida Liang. Advances in multispectral and hyperspectral imaging for archaeology and art conservation. *Applied Physics A: Materials Science and Processing*, 106(2):309–323, feb 2012.

[23] Riley D. Logan, Bryan Scherrer, Jacob Senecal, Neil S. Walton, Amy Peerlinck, John W. Sheppard, and Joseph A. Shaw. Hyperspectral imaging and machine learning for monitoring produce ripeness. In Moon S. Kim, Bryan A. Chin, and Byoung-Kwan Cho, editors, *Sensing for Agriculture and Food Quality and Safety XII*, volume 11421, pages 69 – 82. International Society for Optics and Photonics, SPIE, 2020.

[24] Riley D. Logan and Joseph A. Shaw. Measuring the polarization response of a VNIR hyperspectral imager. In David B. Chenault and Dennis H. Goldstein, editors, *Polarization: Measurement, Analysis, and Remote Sensing XIV*, volume 11412, pages 25 – 31. International Society for Optics and Photonics, SPIE, 2020.

[25] Pieternel A Luning, Theo De Rijk, Harry J Wichers, and Jacques P Roozen. Gas Chromatography, Mass Spectrometry, and Sniffing Port Analyses of Volatile Compounds of Fresh Bell Peppers (Capsicum annuum) at Different Ripening Stages. *Journal of Agricultural and Food Chemistry*, 42:977–983, 1994.

[26] Mehmet Melikoglu, Carol Sze Ki Lin, and Colin Webb. Analysing global food waste problem: Pinpointing the facts and estimating the energy content. *Central European Journal of Engineering*, 3(2):157–164, jun 2013.

[27] Sapan Naik and Bankim Patel. Image processing and machine learning for automated fruit grading system: A technical review. *International Journal of Computer Applications*, 170(9):22–34, 2017.

[28] Paul W Nugent, Joseph A Shaw, Prashant Jha, Bryan Scherrer, Andrew Donelick, and Vipan Kumar. Discrimination of herbicide-resistant kochia with hyperspectral imaging. *J. Appl. Remote Sens*, 12(1):16037, 2018.

[29] Rashmi Pandey, Sapan Naik, and Roma Marfatia. Image processing and machine learning for automated fruit grading system: A technical review. *International Journal of Computer Applications*, 81(16):29–39, 2013.

[30] Ann Peirs, Jeroen Lammertyn, Kristien Ooms, and Bart M. Nicolai. Prediction of the Optimal Picking Date of Different Apple Cultivars by Means of VIS/NIR-Spectroscopy. *Postharvest Biology and Technology*, 21:189–199, 2000.

[31] G Polder, G W A M Van Der Heijden, and I T Young. Spectral Image Analysis For Measuring Ripeness of Tomatoes. *Transactions of the ASAE*, 45(4):1155–1161, 2002.

[32] G Polder, G. W. A. M. van der Heijden, and I. T. Young. Tomato Sorting Using Independent Component Snalysis on Spectral Images. *Real-Time Imaging*, 9:253–259, 2003.

[33] V. Prasanna, T. N. Prabha, and R. N. Tharanathan. Fruit Ripening Phenomena–An Overview. *Critical Reviews in Food Science and Nutrition*, 47(1):1–19, jan 2007.

[34] P Rajkumar, N Wang, G Elmasry, G S V Raghavan, and Y Gariepy. Studies on Banana Fruit Quality and Maturity Stages Using Hyperspectral Imaging. *Journal of Food Engineering*, 108:194–200, 2012.

[35] Resonon. Hyperspectral Imaging Cameras And Systems. Technical report, Resonon, Inc., Bozeman, 2019.

[36] Nayeli Vélez Rivera, Juan Gómez-Sanchis, Jorge Chanona-Pérez, Juan José Carrasco, Mónica Millán-Giraldo, Delia Lorente, Sergio Cubero, and José Blasco. Early detection of mechanical damage in mango using nir hyperspectral images and machine learning. *Biosystems Engineering*, 122:91 – 98, 2014.

[37] Bryan Scherrer, John Sheppard, Prashant Jha, and Joseph A. Shaw. Hyperspectral imaging and neural networks to classify herbicide-resistant weeds. *Journal of Applied Remote Sensing*, 13(4):1 – 15, 2019.

[38] Jacob Senecal. Convolutional neural networks for multi- and hyper-spectral image classification. Master's thesis, Montana State University, Bozeman, MT, 2019.

[39] Jacob Senecal, John Sheppard, and Joseph Shaw. Efficient convolutional neural networks for multi-spectral image classification. In *Proceedings of the IEEE International Joint Conference on Neural Networks (IJCNN)*, 2019.

[40] D C Slaughter and Judith A. Abbott. Applications in Analysis of Fruits and Vegetables. *Near-Infrared Spectroscopy in Agri- culture, Agronomy Monograph no. 44*, (44):1–12, 2004.

[41] J Scott Tyo, Dennis L Goldstein, David B Chenault, and Joseph A Shaw. Review of passive imaging polarimetry for remote sensing applications. *Applied Optics*, 45(22):5453–5469, 2006.

[42] Harshad Vaviya, Ajaykumar Yadav, Vijaykumar Vishwakarma, and Nasim Shah. Identification of artificially ripened fruits using machine learning. *2nd International Conference on Advances in Science Technology (ICAST)*, 2019.

[43] Kumar Venkat. The Climate Change and Economic Impacts of Food Waste in the United States. *International Journal on Food System Dynamics*, 2(4):431–446, dec 2011.

[44] Neil Walton. Utilizing distributions of variable influence for feature selection in hyperspectral images. Master's thesis, Montana State University, Bozeman, MT, 2019.

[45] Neil S. Walton, John W. Sheppard, and Joseph A. Shaw. Using a genetic algorithm with histograph-based feature selection in hyperspectral image classification. In *Proceedings of the ACM Genetic and Evolutionary Computation Conference (GECCO)*, 2019.